JPRS-CST-92-008
30 APRIL 1992



JPRS Report

Science & Technology

China

EXCIMER LASER & FEL RESEARCH

JPRS-CST-92-008
30 APRIL 1992

SCIENCE & TECHNOLOGY

CHINA

EXCIMER LASER & FEL RESEARCH

CONTENTS

Gain Characteristics of Free Electron Laser Operating in the Collective Region
[Lu Zaitong, Zhang Lifen, et al.; ZHONGGUO JIGUANG, No 11, Nov 91].. 1

Spectral Measurement of Raman FEL
[Lu Zaitong, Zhang Lifen, et al.; ZHONGGUO JIGUANG, No 12, Dec 91].. 8

Output Obtained From SG-1 FEL
[QIANG JIGUANG YU LIZI SHU, No 4, Nov 91]..... 14

100J-Class KrF Laser Pumped by Intense Electron Beam
[Wang Naiyan, Shan Yusheng, et al; QIANG JIGUANG YU LIZI SHU, No 4, Nov 91]..... 17

Kinetic Simulation of KrF Laser
[Kang Xiangdong, Shan Yusheng, et al.; QIANG JIGUANG YU LIZI SHU, No 4, Nov 91]..... 30

Multi-Electron-Beam Cerenkov FEL Oscillator
[Wang Qingyuan, Yu Shanfu, et al.; QIANG JIGUANG YU LIZI SHU, No 4, Nov 91]..... 39

On-Line Measurements of Pulsed Electron Beam Emittance
[Zhu Dajun, Huang Sunren, et al.; QIANG JIGUANG YU LIZI SHU, No 4, Nov 91]..... 45

Beam Quality Improvement Using Collimating Apertures
[He Peiai, Cheng Nianan, et al.; QIANG JIGUANG YU LIZI SHU, No 4, Nov 91]..... 55

Electromagnetic-Wave-Pumped FEL Studied
[Yin Yuanzhao; DIANZI KEXUE XUEKAN, No 6, Nov 91]..... 62

Nation's First EMW-Pumped FEL Experimental System Completed
[SICHUAN RIBAO, 6 Feb 92]..... 68

100-Watt High-Repetition-Rate XeCl Excimer Laser Developed
[Wei Zaozhi; ZHONGGUO DIANZI BAO, 28 Feb 92]..... 69

100J-Class KrF Excimer Laser Passes CNNC-Organized Expert Appraisal
[Chang Jiachen; ZHONGGUO KEXUE BAO, 17 Mar 92]..... 70

Tapered Wiggler Technique Used in Low-Energy-E-Beam Raman FEL
[Zhao Donghuan, Wang Jian; ZHONGGUO JIGUANG, No 1, Jan 92]..... 71

Gain Characteristics of Free Electron Laser Operating in the Collective Region

92FE0283A Shanghai ZHONGGUO JIGUANG [CHINESE JOURNAL OF LASERS] in Chinese
Vol 18 No 11, Nov 91 pp 801-805

[Article by Lu Zaitong [7120 6528 6639], Zhang Lifen [1728 4539 5358], Zhao Donghuan [6392 2639 3562], Wang Mingchang [3769 2494 1603], and Wang Zhijiang [3769 0037 3068] of Shanghai Institute of Optics and Fine Mechanics (SIOFM) of the Chinese Academy of Sciences: "Study of Gain Characteristics of Free Electron Laser Operating in the Collective Region"; MS received 24 Jan 90, a project funded by the National Natural Science Foundation]

[Text] Abstract

The gain characteristics of a collective free electron laser (FEL) operating in super-radiant mode have been studied by varying the length of the interaction zone and the strength of the pumping magnetic field. Any arbitrary interaction length can be obtained by using an axially movable "kicker" magnetic field to deflect the electron beam (e-beam). It was experimentally found that radiant gain of a collective FEL appears to obey 1.7th power of the pumping magnetic field. The gain factor was obtained within the range of 0.4 dB/cm to 1.38 dB/cm.

I. Introduction

The FEL wave amplification process is achieved through the interaction between a relativistic e-beam and a spatial magnetic field (i.e., wiggler magnetic field). The wiggler magnetic field provides the coupling between the e-beam and the electromagnetic radiation field to form a ponderomotive force along the e-beam axis. A collective FEL has a space-charge potential comparable to the potential corresponding to the ponderomotive force. Hence, it is necessary to take its interaction into consideration. Therefore, a collective FEL may be considered as the coupling of the negatively energized space-charge wave and the positively energized electromagnetic wave in a wiggler magnetic field. An axial magnetic field may be used to guide the transport of an intense relativistic e-beam (of the order of kA) in this type of FEL. Furthermore, this axial magnetic field can significantly increase the gain of the radiation. In such a complex system, it is helpful to study the dependence of gain characteristics upon various parameters in order to obtain a profound understanding of the operating mechanism and unique features of

the collective FEL. This paper discusses the relation between its gain and the strength of the wiggler magnetic field and the interaction length.

II. Experimental Apparatus

Figure 1 shows the schematic diagram of the collective FEL used to study the gain characteristics.

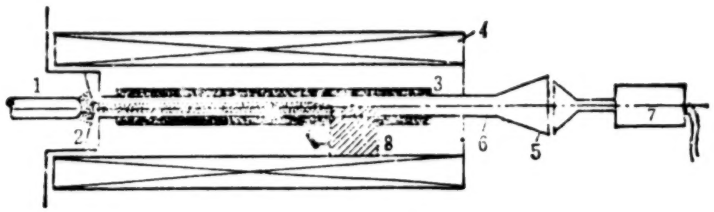


Figure 1. Configuration of a Raman Free Electron Laser To Measure Gain Characteristics

1. Cathode; 2. Anode; 3. Wiggler magnet; 4. Guide magnetic field; 5. Microwave horn; 6. Drift tube; 7. Calorimeter; 8. Movable "kicker" magnet

A pulse linear accelerator provides an intense 0.4-0.45 MeV e-beam at near 1 kA.[1] Under the guidance of a 10 kG magnetic field, the e-beam passes through a 6-mm-diameter aperture at the anode and enters the interaction zone inside a 20-mm-inner-diameter stainless steel tube. On the outer wall of the drift tube, a right-handed doubly-wound coil is used to generate the wiggler magnetic field. The pulse wiggler magnetic field is continuously tunable from 0 to 2 kG. The wiggler field has 59 periods and each period is 22 mm. The first five periods at the inlet is the adiabatic transition section. In order to avoid magnetic field fluctuation at the end, a 1-mm-thick, 30-mm-diameter circulating ring is added there.

The interaction length is varied by using an iron-core kicker inside the solenoid pulse magnet, which generates the guiding magnetic field. It alters the uniform magnetic field inside the solenoid to cause a local deflection. Once this local deflection reaches a certain degree, the guided e-beam would be so severely deflected that it hits the wall of the drift tube and is absorbed by the wall. By moving the position of the kicker, it is possible to obtain any interaction length. The kicker is a half circle ring with an inner diameter of 35 mm and outer diameter of 130 mm. It can be moved along the inner wall of the solenoid and be fixed at any position.

Once passing through the interaction zone, after the amplified radiation signal is transmitted a certain distance in the round waveguide, it outputs through a microwave horn. After reception by the microwave horn and high-pass filtering, the signal goes into a radiometer or is detected by a crystal detector. The time-dependent millimeter signal is displayed on an oscilloscope.

III. Measurement of Deflecting Magnetic Field and Determination of Interaction Length

As described earlier, the deflecting magnetic field is obtained by inserting an iron-core kicker inside the guiding magnetic coil. Figure 2 shows the results of measured axial magnetic field in the interaction zone after the kicker is introduced. It shows that the kicker only affects the local magnetic field strength in its vicinity. The position where the axial magnetic field is 90 percent of its normal value is at 2 cm in front of the end of the kicker. In order to verify the effect of the deflecting magnetic field on e-beam transport and to more accurately determine the interaction length, we measured the e-beam cross-section distribution at several points along the axis using acid-sensitive plates with the kicker in place. The deflection of the e-beam can be estimated from the displacement of the target image. Figure 3 [not reproduced] shows a photograph of the e-beam cross-section target image at three places. Figure 3(1) shows the cross-section target under normal e-beam transport, i.e., when the kicker does not play a role. The position of measurement is 5 cm in front of the end of the kicker. At 2 cm in front of the kicker, the center of e-beam cross section is off to the side by 2-3 mm relative to the e-beam axis (see Figure 3(2)). At 2 cm behind the rear end of the kicker, the plate can no longer show the target (see Figure 3(3)). Hence, the e-beam must have hit the wall before this position. A significant surge of X-ray dosimetry measurement near this position confirmed this point.

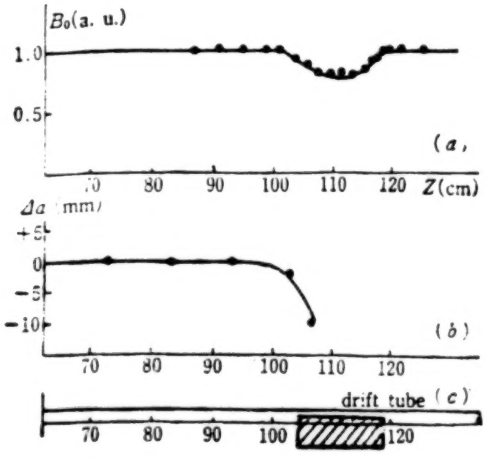


Figure 2. Axial Magnetic Field Distribution and Deflected Distance of e-Beam Versus "Kicker" Magnet Position

(a) axial magnetic field distribution; (b) deflected distances of e-beam from central axis; (c) corresponding position of the "kicker" magnet

Based on the magnetic field measurements and target photograph discussed above, it can be concluded that the uncertainty of interaction length as determined by the end position of the kicker is less than ±2 cm.

IV. Radiation Gain Characteristics

Derivation of the gain of an FEL under the influence of a wiggler field and a guiding field from the Vlasov equation and Maxwell equations has been discussed in the literature.[2-4]

If the pumping period is shorter than the system length, then the gain of radiation with an interaction length L at a frequency $\omega \simeq (K + K_W)v_z$ can be expressed as:

$$G_L \simeq \beta_W^2 \frac{\omega_b^2 L^2 K}{16\gamma_0 \gamma_Z^2 v_{11}^2} \left[1 - \frac{\gamma_Z^2 \beta_W^2 \Omega_0}{\Omega_0(1+\beta_W^2) - K_W v_{11}}\right] \frac{\partial}{\partial x}\left[\frac{\sin x}{x}\right]^2 \tag{1}$$

In equation (1), ω and K are the frequency and wave number of the electromagnetic wave, respectively; ω_b is the plasma characteristic frequency and $\omega_b^2 = 4\pi n_b e^2/m$ (n_b is electron density); $\beta_W = v_\perp/v_z$, which is the ratio of the lateral component of electron velocity to the axial component of electron velocity; $K_W = 2\pi/\lambda_W$, where λ_W is the period of the wiggler; γ_0 is the relativistic factor, whose axial component $\gamma_Z = (1-\beta_Z^2)^{-1/2}$; v_z is the axial electron velocity; $x \equiv (\omega/v_z - K - K_W)L/Z$; the cyclotron frequency of an electron in the axial magnetic field B_0 is $\Omega_0 \equiv eB_0/\gamma mc$; and L is the gain length.

G_L has an extreme value at $x \cong \pm 1.3$, and $\frac{\partial}{\partial x}(\sin x/x)^2 \cong \mp 0.54$. The peak gain value is:

$$(G_L)_{max} \simeq \pm 0.0675\, \beta_W^2 \frac{\omega_b^2}{\gamma_0 K_W^2 C^2} (K_W L)^3 \left[1 - \frac{\gamma_Z^2 \beta_W^2 \Omega_0}{\Omega_0(1+\beta_W^2) - K_W v_z}\right] \tag{2}$$

The frequency it corresponds to is:

$$\omega \simeq 2\gamma_Z^2 K_W v_z (1 \pm 2.6/K_W L) \tag{3}$$

Equation (2) shows that when $K_W v_z \simeq \Omega_0(1+\beta_W^2)$, there is a singularity point near which the gain is substantially higher. Hence, the introduction of a guiding field can increase the gain. Equation (3) shows that peak gain values may occur at two different frequencies.

The effect of the axial magnetic field on gain can be briefly summarized as follows.[3] When $\Omega_0 \sim K_W v_z$, the gain rises sharply because the lateral velocity increases rapidly ($v_\perp \equiv \Omega_W v_z/\Omega_0 - K_W v_z$). When $\Omega_0 < K_W v_z$, it operates on branch I and the gain rises with increasing axial velocity. It operates on branch II when $\Omega_0 > K_W v_z$. For a mono-energetic beam, there is a critical value $\Omega_0' = \frac{K_W v_z}{1-\beta_W^2}$ for which the gain varies in a pattern similar to that of branch I when $\Omega_0 > \Omega_0'$. When $\Omega_0 < \Omega_0'$, the gain rises with decreasing axial field strength.

As for the relation between gain and wiggler field, the small-signal gain increases with the square of wiggler field strength when there is no axial

field, i.e., proportional to the square of $v_\perp$. However, with a guiding field, the situation is very complicated. The gain does not vary monotonically with respect to Ω_W/K_WC. When the transverse field parameter is small, the gain does increase according to the square rule. It peaks at a certain field parameter and then falls rapidly.

V. Experimental Results on Gain Characteristics

Experimental determination of the gain can be accomplished by measuring the radiation output characteristics with various interaction lengths and under different wiggler fields. Figure 4 shows the laser radiation as a function of wiggler magnetic field at four interaction lengths. Under our experimental conditions, when the wiggler field is increased to over 1,000 G, the output power apparently falls. The more mono-energetic the e-beam is, the steeper this decline becomes. The sharp drop can be considered to take place near the theoretical singularity point. The relation between output and interaction strength can be experimentally determined by fixing the pumping condition (see Figure 5). The figure shows that at low pumping rates, the output gradually saturates with increasing interaction length. At high pumping rates, it reaches saturation faster. The saturation power varies between 5 and 10 MW. The length over which the gain increases exponentially is approximately 50 cm, depending upon the pumping intensity. After reaching saturation, the radiation fluctuates up and down as the interaction length increases. Reference 5 believes that this is due to phase condition for synchronous electrons in a ponderous potential well. In order to avoid reaching saturation too soon and to improve the conversion efficiency of the radiation output, the wiggler field intensity or wiggler period may be made variable. This way allows electrons that lost their energy to remain in resonant condition. It also allows the electromagnetic wave to obtain more energy from the e-beam to improve the conversion efficiency.

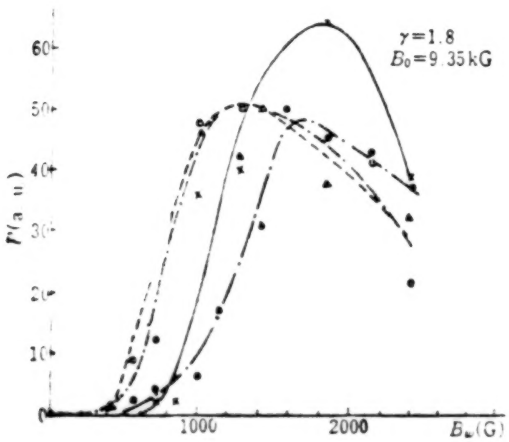


Figure 4. mm-Wave Radiation Power Versus Wiggler Magnetic Field at Various Interaction Lengths

×-interaction length L=30 cm; ●-L=40 cm; ○-L=60 cm; △-L=80 cm

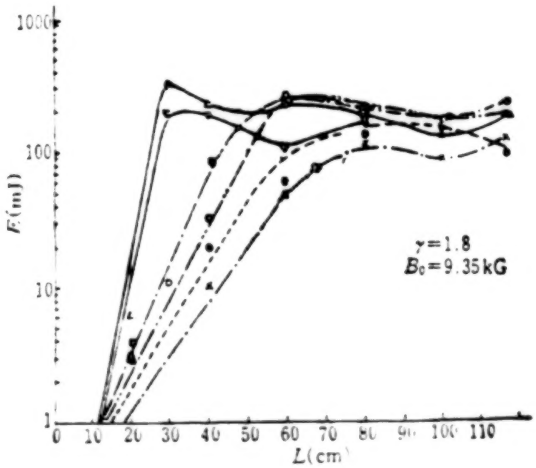


Figure 5. Interaction Length Versus Radiation Output Energy

B_w: ×-560G; ●-700G; ○-980G; ■-1260G; △-1.8kG; ▽-2.3kG

Figure 4 also shows that the wiggler field strength corresponding to peak power gradually decreases as the interaction length increases. This illustrates the gain versus wiggler field relation. Figure 6 shows the experimentally measured gain versus wiggler field curve. As it illustrates, the gain begins to fall after exceeding a certain pumping intensity. This is consistent with the theory regarding a collective FEL.

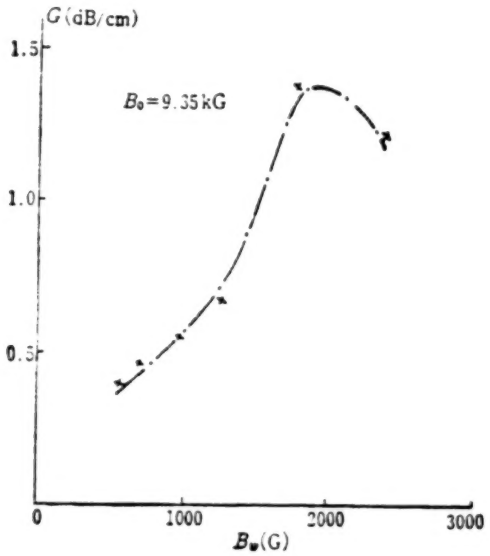


Figure 6. Growth Rate as a Function of Wiggler Magnetic Field for $\gamma \approx 1.8$, $B_0 \approx 9.35$ kG

VI. Conclusions

(1) Small-signal gain length versus pumping intensity curve (Figure 5) shows that the small-signal gain length is approximately 70 cm. Under a high pumping magnetic field, it is approximately 30 cm. In order to expand the linear gain region under the same pumping strength, a variable wiggler field may be employed to improve electron conversion efficiency.

(2) Our experiment met the condition of $K_w v_z < \Omega_0$. The device operates on branch II. Theoretical analysis points out that the gain increases with rising Ω_W. A peak occurs under a specific pumping condition. Afterward, it falls rapidly. This point was experimentally verified. The experiment was conducted with both a pumping field and a guiding field present. At low pumping rates, the gain increases rapidly as a function of the 1.7th power of the pumping field. It is slightly different from the theoretical square rule. The gain peaks at 1.38 dB/cm and then begins to fall. This is also consistent with the theory. The smaller power of rise and slower drop may be due to the finite width of the energy spectrum of the e-beam.

References

1. Lu Zaitong et al., GUANGXUE XUEBAO [ACTA OPTICA SINICA], Vol 9, No 9, 1989, pp 780-786.

2. H. P. Freund et al., PHYS. REV. A, Vol 24, No 4, 1981, p 1965.

3. L. Friedland et al., PHYS. REV. A, Vol 25, No 5, 1982, pp 2693-2706.

4. H. P. Freund et al., PHYS. REV. A, Vol 26, No 4, 1982, pp 2004-2015.

5. T. J. Orzechowski et al., PHYS. REV. LETT., Vol 57, No 17, 1986, pp 2172-2175.

Spectral Measurement of Raman FEL

92FE0380A Shanghai ZHONGGUO JIGUANG [CHINESE JOURNAL OF LASERS] in Chinese Vol 18 No 12, Dec 91 pp 881-884

[Article by Lu Zaitong [7120 6528 6639], Zhang Lifen [1728 4539 5358], Wang Mingchang [3769 2494 1603], and Wang Zhijiang [3769 0037 3068] of Shanghai Institute of Optics and Fine Mechanics, the Chinese Academy of Sciences: "Spectral Measurement of Raman FEL"; Funded by the National Natural Science Foundation, MS received 10 Apr 90]

[Text] Abstract

Preliminary results of the emission spectrum of a Raman free electron laser (FEL) operating under super-radiation condition obtained with a microwave grating spectrometer are reported. Tunability of the millimeter-wave FEL was observed. Experimentally, it was found that the central frequency of the emission spectrum decreased with increasing strength of the wiggler magnetic field. This is consistent with the theoretical prediction concerning the effect of waveguide mode on a collective FEL.

I. Introduction

High power millimeter-wave emission from a Raman FEL is an important source of high power millimeter waves. Since high power millimeter-wave emission has a wide range of scientific and military applications, in-depth study of the Raman FEL has become an important aspect in the development of high power millimeter-wave devices.

Our earlier experimental work on the Raman FEL[1,2] has fully demonstrated its unique characteristics such as high power, high efficiency and tunability. The emission wavelength was measured by a cut-off waveguide method.[3] It was determined that the laser emission is in the K_a band. In addition, the same method was used to observe its tunability.[1] In order to study the emission mechanism and physics involved in depth, it is necessary to obtain more accurate data regarding the emission frequency and its spectral distribution. To this end, we developed a high power millimeter-wave spectrometer to measure the spectral characteristics of the Raman FEL.

II. Coupling Frequency

The working frequency of a collective FEL can be derived from the dispersion relation of the negative energy static electron beam mode (1) and the dispersion equation of the electromagnetic waveguide mode (2), i.e.

$$\omega = (K + K_w)v_z - kv_z \tag{1}$$

$$\omega^2 = c^2K^2 + \omega_{co}^2 \tag{2}$$

where ω and K represent the frequency and wave number of the emission, respectively. ω_{co} is the cut-off frequency in the waveguide; $K_w \equiv 2\pi/\lambda_w$ is the wave number of the wiggler and kv_z is the effective plasma frequency. Under our experimental conditions, $(1-\gamma_z^2 v_\perp^2/c^2)\Omega_0 < K_w v_z < \Omega_0$. In this case, the effective plasma frequency is an imaginary number which has no contribution to the real part of the static electron beam mode. Hence, equation (1) can be rewritten as:

$$\omega = (K + K_w)v_z \tag{3}$$

Therefore, the coupling frequency that satisfies equations (2) and (3) can be expressed as follows:

$$\omega \cong \gamma_z^2 K_w v_z \left[1 \pm \left(\beta_z^2 - \frac{\omega_{co}^2}{\gamma_z^2 \cdot K_w \cdot c}\right)^{\frac{1}{2}}\right] \tag{4}$$

If the effect of waveguide mode can be neglected, then

$$\omega \approx \beta_z(1+\beta_z)\gamma_z^2 \cdot K_w \cdot c \tag{5}$$

where $\gamma_z \equiv (1/1-\beta_z^2)^{\frac{1}{2}}$; $\beta_z \equiv v_z/c$, where v_z is the axial speed of the electron; $\Omega_0 \equiv eB_0/\gamma \cdot m \cdot c$, where m is the rest mass of the electron; γ is the relativistic factor and c is the speed of light.

III. Experimental Setup

Figure 1 shows the experimental system used to measure the emission spectra of a Raman FEL.

The energy of the electron beam emitted by the plasma in the diode of the pulsed linear accelerator is 0.4-0.45 MeV. The electron beam current in the interaction zone of the drift tube is close to 1 kA.[2] The electron beam is guided into the interaction zone through a 12-mm-thick anode with a 6-mm-diameter hole or an emissivity selector by means of a 10 kG guiding magnet. The wiggler in the interaction zone is continuously tunable within 0-2 kG. The wiggler coil is directly wound around the outer wall of the drift tube. In our spectral measurements, the interaction zone was chosen to be 790 mm long. The FEL emission goes through the waveguide and comes out of the output horn.

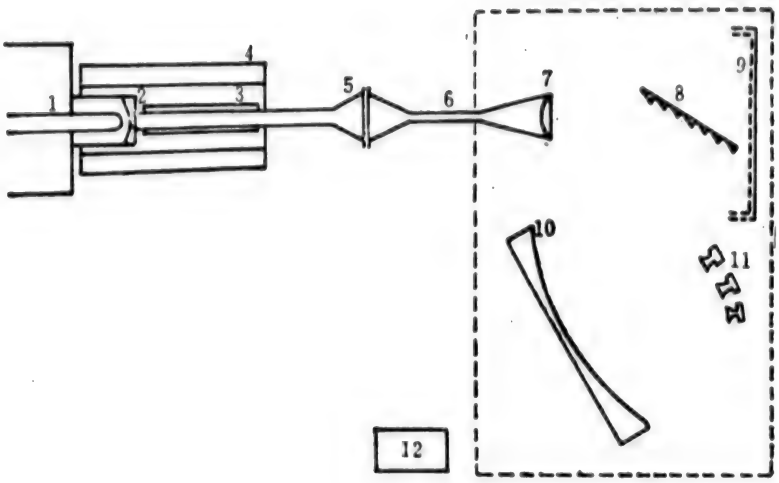


Figure 1. Schematic Diagram of the Radiation Spread Measurement for a High Power Pulsed mm-Wave Free Electron Laser

1. cathode; 2. anode; 3-wiggler magnet; 4. guide magnet; 5. output horn; 6. input horn with the cut-off waveguide; 7. microwave lens; 8. reflection grating; 9. absorption material; 10. cylindrical mirror; 11. detector; 12. mm-wave measurement device

In order to reach a specific wavelength resolution using the millimeter-wave spectrometer to measure the FEL emission, the beam is first expanded to a 100-mm-diameter cross section and then collimated by a convex tetrafluoroethylene lens. The collimated parallel beam is shone at an incident angle α onto a microwave grating with a grazing angle of $\theta = 30°$. The microwave grating constant is $d = 7.5$ mm. The number of grooves is $N = 30$ and the typical angle of incidence is $\alpha = 60°$. Corresponding to such grating conditions, the wavelength covers a range of 5 mm to 10 mm. The radius of curvature of the cylindrical concave mirror is 1.5 m, and the mirror is 20 cm high. It is made of polished copper skin on a hard substrate. The diffracted light is focused by the cylindrical mirror to enter various receiving horns corresponding to different wavelengths. Through waveguide K_a, it reaches the attenuator and high-pass filter inside a shielded chamber. The millimeter-wave signal is picked up by a crystal detector and displayed on an oscilloscope. If there is not enough equipment to simultaneously measure several millimeter-wave signals at different wavelengths, then it is not possible to obtain the spectral distribution of a super-radiation Raman FEL in a single measurement. However, when the laser output is relatively stable, i.e., the reproducibility is good, then satisfactory spectral distribution might be obtained by using a rotating microwave grating monochromator.

From the design parameters and precision of machined components of the spectrometer, it is possible to estimate the wavelength resolution and spectral distribution error of the device. If the beam is parallel from the lens to the microwave grating, with a fixed incident angle α, from angular dispersion of $d\beta/d\lambda$ and half base width $\Delta\beta = \lambda/N \cdot d$, the wavelength resolution can be expressed as $\Delta\lambda = \lambda/m \cdot N$, where λ is the wavelength of the measured millimeter waves, m is the order of interference which is chosen to be 1,

N is the number of grooves, and α is the angle of incidence. By substituting the actual design parameters and choosing m = 1, the wavelength resolution at the actual central wavelength of 8 mm is $\Delta\lambda = \lambda \cdot d \cos\alpha/100 = 0.3$ mm.

It is estimated that the machining error of the microwave grating constant d is < 0.1 mm. Hence, the wavelength error is < 0.1 mm. The incident angle error is determined by the precision of the adjustment mechanism. The mechanism we used has an adjustment error of 4'. This causes a wavelength reading error of 0.02 mm, which is far less than the wavelength resolution.

The wavelength resolution error caused by the width of the receiver is $d\lambda = 2 \cdot d \cdot \cos\beta \cdot dl/r$, where d is the microwave grating constant, β is the corresponding angle of diffraction, dl is the distributive width of diffraction angle $d\beta$ on the reception surface, and r is the distance between the grating and the focusing mirror. Based on actual structural parameters, it is possible to calculate that the resolution error caused by the width of the receiver at the central wavelength is 0.06 mm. The overall error is $\Delta\overline{\lambda} \approx 0.32$ mm.

IV. Experimental Results and Discussion

The objectives of this preliminary experiment of measuring the spectra of a Raman FEL with a microwave spectrometer are to verify the theoretical prediction concerning its central frequency and to observe its spectral distribution. The spectrum shown in Figure 2(a) corresponds to a guiding magnetic field B_0 = 9.35 kG and wiggler field B_w = 980 G with $\beta_\perp \approx 0.3$. Figure 2(b) corresponds to B_0 = 9.35 kG, B_w = 1260 G and $\beta_\perp \approx 0.34$. Based on the coupling frequency equation (4), the coupling frequencies for the TE_{11} mode under these two conditions are 44 GHz and 38.9 GHz, respectively.

Furthermore, they are 41.7 GHz and 36.3 GHz for the TM_{01} mode, respectively. The peaks shown in Figure 2 correspond to 42.8 GHz and 37.5 GHz, respectively. The discrepancy might be due to errors related to the experimental parameters used in the calculation. Another reason might be the resolution error of the spectrometer itself.

Figure 3 shows the calculated emission frequency variation pattern of a superradiation collective FEL with a fixed electron parameter and guiding magnetic field B_0, i.e., γ = 1.8 and B_0 = 9350 G. Line a represents the frequency variation without considering the waveguide, line b represents the frequency variation in the TE_{11} mode, and line c represents the frequency characteristics in the TM_{01} mode. Points marked in the figure represent peak frequencies measured under those conditions with B_w at 980 G and 1260 G. Two experimental points happened to fall between the two lines for TE_{11} and TM_{01}. Hence, further experimental work is required to acquire more data points to pinpoint the cause of error in order to make the determination of radiation mode more accurate.

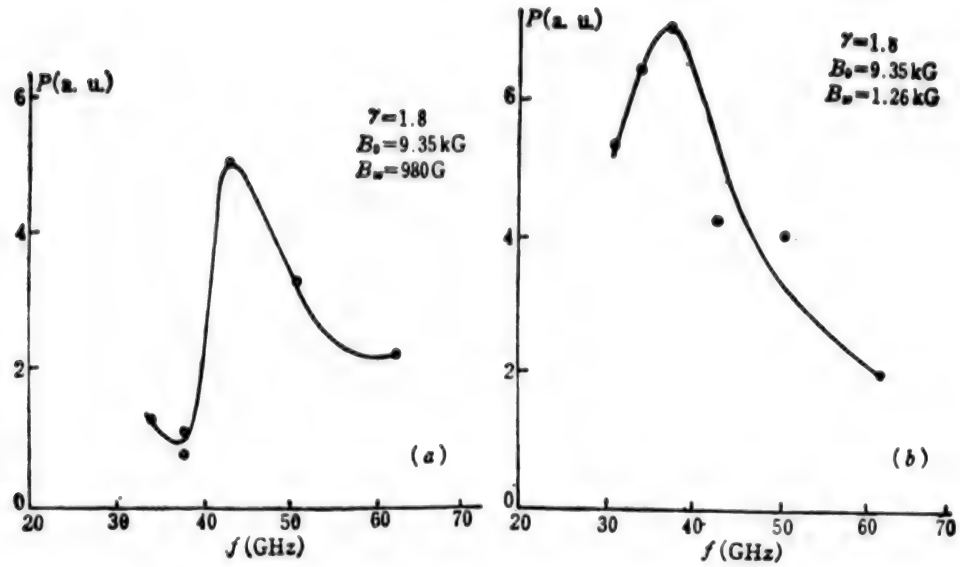


Figure 2. Frequency Spread of a Raman Free Electron Laser as a Super-Radiation Amplifier

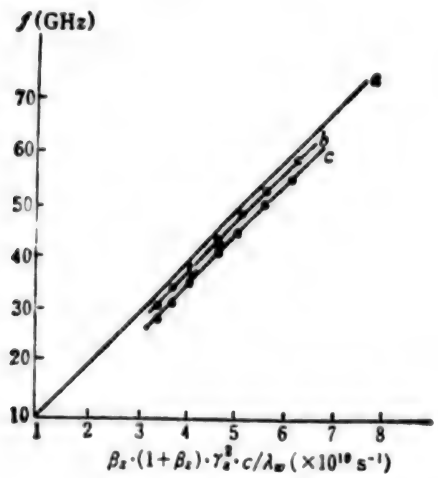


Figure 3. Emission Frequencies Versus $\beta_z \cdot (1+\beta_z) \cdot \gamma_z^2 \cdot c/\lambda_w$

a. without waveguide; b. TE_{11} mode; c. TM_{01} mode

Preliminary measurement of spectral distribution of a millimeter-wave super-radiating FEL reveals that the frequency variation as a function of experimental parameters is essentially consistent with the theoretical prediction. In addition, the FEL emission from a multi-mode circular waveguide is in one of the two lowest-order modes (i.e., TE_{11} and TM_{01}). The line width is 0.3, which indicates that the mutual interaction gain bandwidth is relatively wide. For Raman FELs operating in type-II orbit, this experimental result is in agreement with the theory. Preliminary spectral measurement also points out the tunability of the FEL.

References

1. Chu Cheng [5969 2052] et al., ZHONGGUO KEXUE, Series A [SCIENTIA SINICA], No 11, 1987, pp 1211-1216.

2. Lu Zaitong et al., GUANGXUE XUEBAO [ACTA OPTICA SINICA], Vol 9, No 9, 1989, pp 780-786.

3. Chu Cheng, et al., ZHONGGUO JIGUANG [CHINESE JOURNAL OF LASERS], Vol 13, No 8, 1986, pp 41-44.

Output Obtained From SG-1 FEL

92P60125A Chengdu QIANG JIGUANG YU LIZI SHU [HIGH POWER LASER AND PARTICLE BEAMS] in Chinese Vol 3 No 4, Nov 91 inside front cover

[Article by SFEL Team: "Shuguang-1 Free Electron Laser Facility Achieves Output"]

[Text] In order to conduct basic physical research into the free electron laser (FEL), the China Academy of Engineering Physics (CAEP) has designed and constructed the Shuguang-1 (SG-1) FEL facility (SFEL), which achieved output for the first time on 17 September 1991.

The SFEL electron-beam source is a 3.3 MeV induction linear accelerator (induction linac) with a beam intensity of 2 kA. In order to match the induction linac to the FEL interaction region, one needs to insert between the accelerator and the wiggler a collimator and three quadrupole devices, which form the beam modulation segment. The beam modulation segment or region has a total length of 9.5 m, and contains three current-detection assemblies used for on-line monitoring of the beam. The wiggler has the structure of an electromagnet, with a specially polished parabolic cylinder installed on the end face of the magnetic pole in order to better focus the two surfaces of the electron beam. An external view of the SFEL is shown in Figure 1.

The output signal is measured and recorded with an 8-mm wave detector diode and an HP 54502A oscilloscope. The detector diode is carefully installed into a metal cylinder to forestall space electromagnetic-wave interference. Figure 2 shows an experimentally measured typical signal waveform. To maintain the signal's frequency range, one needs to install between the detector diode and the receiving horn a bandpass filter with a special frequency range. Figure 3 shows the signal waveform after bandpass filtering. The bandpass filter parameters are: center frequency f = 35.5-36.5 GHz, insertion loss is about 2 dB, and out-band attenuation exceeds 20 dB.

The experimentally obtained power level and frequency range are in good agreement with the values predicted in a numerical simulation. The experiment's operating parameters and the aforementioned results are combined in Table 1.



Figure 1. External View of SFEL

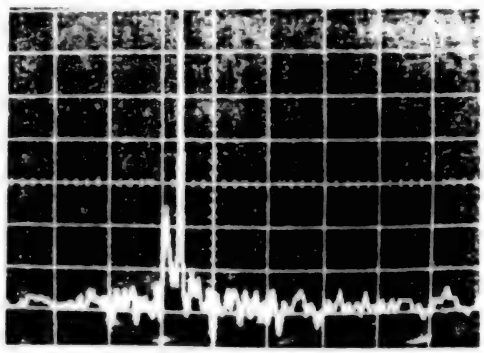


Figure 2. Typical Signal Waveform
(Vert. axis 100 mV/div, horiz. axis 100 ns/div)

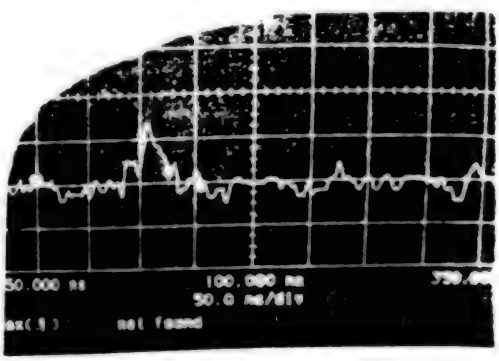


Figure 3. Waveform After Bandpass Filtering
(Vert. axis 100 mV/div, horiz. axis 50 ns/div)

Table 1. Experimental Operating Parameters and Initial Results

Electron beam	Wiggler	Waveguide	Output signal
$E_e \approx 3$ MeV	$L_w = 2.64$ m	a x b = 9.8 x 2.9 cm	I = 50-150 A
I = 50-100 A	$\lambda_w = 11$ cm	wavemode = H_{01}	P_0 = 300-700 mW
$\epsilon_n < 0.47\pi$ cm-rad	$B_w = 2.6$ kGs		f = 35.5-36.5 GHz
$\Delta E_e/E_e \approx 4\%$	$\Delta B_w/B_w \approx 0.7\%$		$\tau = 30$ ns
$\tau = 50$ ns	$\alpha = k_y/k_x = 2$		
	$\lambda_{out} = 1.5\ \lambda_w$		

100J-Class KrF Laser Pumped by Intense Electron Beam

92FE0307A Chengdu QIANG JIGUANG YU LIZI SHU [HIGH POWER LASER AND PARTICLE BEAMS] in Chinese Vol 3 No 4, Nov 91 pp 411-420

[Article by Wang Naiyan [3769 0035 1750], Shan Yusheng [0830 3768 3932], Zeng Naigong [2582 0035 1562], Zhou Chuangzhi [0791 0482 1807], Ma Weiyi [7456 4850 5030], Yang Dawei [2799 1129 3634], Wang Xiaojun [3769 2400 6511], Wang Ganchang [3769 3227 2490] et al. of the China Institute of Atomic Energy (IAE): "100J-Class KrF Laser Pumped by Intense Electron Beam"; MS received 24 Aug 91, revised 9 Oct 91]

[Text]

Abstract

The major characteristics, pulsed power technology and laser oscillator technology associated with an intense-electron-beam-pumped 100 J KrF laser currently under construction at IAE are described.

Key Words: KrF laser, intense electron beam, pulsed power technology, large-area electron beam diode, laser oscillator.

I. Introduction

As a potential candidate for an inertial confinement fusion (ICF) driver, the KrF laser is actively being developed in the United States, UK, Japan, USSR, Canada and China. Table 1 is a list of KrF laser systems being pursued internationally for ICF. During the course of design and development of the 100 J KrF laser facility at IAE, we encountered a great deal of physics- and engineering-related problems such as pulsed power technology, large-area electron beam (e-beam) generation, e-beam transport efficiency and the anode-film and main-film penetration efficiency, e-beam energy deposition in lasing media, and energy output of laser oscillator. This paper focuses on pulsed energy technology, generation of an unpinched intense relativistic e-beam and laser energy output.

The development of a 100 J KrF excimer laser began in 1986. An intense e-beam accelerator was constructed in 1982. Its specifications are: 1 MeV in electron energy, 80 kA in e-beam current and 80 ns in pulse width. It was built to conduct basic research on e-beam-induced fusion.[1,2] In 1985, the direction was shifted from e-beam-induced fusion to KrF laser-induced fusion.

On the basis of the original accelerator, a large-area unpinched relativistic intense e-beam diode was developed to replace the focused e-beam diode. Furthermore, this large-area unpinched e-beam was used to pump the lasing medium. In 1985 and 1989, laser energy output reached 13 J and 30 J, respectively.[4,5] By 1991, it reached 100 J. In order to obtain 100 J, the original accelerator and laser cavity had to be rebuilt. Experimental conditions to obtain the three levels of laser energy output are listed in Table 2.

Table 1. KrF Laser Technology Is Being Pursued Internationally for ICF

Laser system	Status	Laser energy (kJ)	Power (W)
Aurora (Los Alamos)	1985	10	2×10^{13}
	1988	1	2×10^{14}
	1989	4	10^{15}
Nike (NRL)	1989	0.01	
	~1993	2	
Sprite (Rutherford)	1983	0.2	3×10^{12}
Super-Sprite (Rutherford)	1994	10	variable
Ashura (ETL, Japan)	1988	0.5	5×10^{12}
Super-Ashura (ETL, Japan)	1993	1	10^{14}
Rapier B (U of Alberta)	1988	0.1	
		1 (proposed)	
Heaven (IAE of China)	1989	0.03	6×10^{11}
	1991	0.1	2×10^{12}

Table 2. Experimental Conditions for Getting Three Levels of Laser Energy

laser energy	Status	electron beam parameter		laser oscillator parameter	
13J (KrF) 5J (XeF)	1985	450keV 100ns	45kA 8×38cm	∕70mm	1.8Liters
30J (KrF)	1989	600keV 100ns	70kA 7.2×37cm	∕100mm	3.6Liters
100J (KrF)	1991	600keV 100ns	240kA 12×75cm	∕200mm	23Liters

The energy stored in the Marx generator is 34 kJ. The impedance of the Blumlein transmission line is 6.5Ω. The Blumlein transmission line is charged by the Marx generator in approximately 900 ns. After the pre-pulse switch is triggered, the Blumlein transmission line begins to charge up the taper transmission line. The impedance of the taper transmission line changes from 6.2Ω to 2.5Ω. The cathode area of the large-area e-beam diode

is 12 x 75 cm. The anode-to-cathode distance is 2 cm. It has reached 600 keV in electron energy, 240 kA in e-beam current and 200 A/cm^2 in e-beam current density.

The gas lasing medium is a 2.5 atm mixture of 89.6 percent Ar, 10 percent Kr and 0.4 percent F_2. The reflectance of the output coupler of the optical resonant cavity and the reflectance of the reflective mirror are 30 and 98 percent, respectively. The lasing length in the cavity is 75 cm and window diameter is 20 cm. The window material is made of quartz.

The laser energy output is measured by a SCIENPECH38-8UV5 calorimeter. The laser pulse profile is measured by two GD-51 photodiodes. The laser spectrum and fluorescence are measured by a 2 m plane grating spectrograph and read by a 3CS microdensitometer. The laser pulse is 60 ns wide, the center wavelength is 248 nm, and the FWHM (full width half maximum) is 0.7 ns. The relation between laser energy output and pumping e-beam current density is calculated for three different cavity sizes. The results are in good agreement with our experimental data.

II. Pulsed Power Technology

The 0.14 TW [terawatt] intense electron pulse accelerator is a modification of the original 0.08 TW accelerator. The new specifications are 0.14 TW, 10 kJ, 0.6 MV, 240 kA and 100 ns. The accelerator primarily consists of four components: a Marx generator immersed in transformer fluid, Blumlein transmission line, taper transmission line and unpinched large-area intense e-beam diode.

As shown in Figure 1 [photograph not reproduced], the Marx generator has 20 capacitors. Each capacitor has a capacitance of 0.7 μF and a breakdown voltage of 100 kV. In addition, there are 10 spherical gap switches. When the capacitors are charged to 70 kV, the energy stored in the Marx generator is 34 kJ, the series capacitance is 35 nF and the inductance is 9 μH. The trigger signal for the first three spherical gap switches comes from a small Marx generator. The remaining switches are instantaneously tripped by overvoltage. In order to enhance the stability of the Marx generator, another trigger method is also used in addition to instantaneous overvoltage. A trigger voltage from two tripped spherical gaps in front is coupled to the spherical gap by water resistance to ensure its breakdown. This method significantly reduces the probability of premature firing. The probability of firing before reaching 70 kV is less than 1 percent. The Marx generator works reliably at one-half the breakdown voltage of the spherical gap.

The voltage amplitude of the Marx generator and its stability are satisfactory. Figure 2 [photograph not reproduced] shows the superposition of the output waveforms of 21 experiments.

Figure 3 shows the Blumlein transmission line. The outer cylinder is 126 cm in diameter and the middle cylinder is 91 cm in diameter. These two cylinders form a 2.2Ω outer Blumlein transmission line. The inner cylinder is 48 cm in diameter. The middle and inner cylinder form a 4.3Ω inner Blumlein

transmission line. The length of the transmission line is 70 ns. The charging time of the Blumlein transmission line by the Marx generator is 0.9 μs. After the charging voltage reaches 1.0 MV, the main switch breaks down. A voltage wave immediately travels along the Blumlein transmission line. Upon reaching the pre-switch, it breaks it down and the taper transmission line is charged. The impedance of the taper transmission line changes from 6.5 to 2.5Ω. Theoretical computation indicates that the voltage transmission efficiency of the taper transmission line is $\eta_v \propto (Z_2/Z_1)^{\frac{1}{2}}$, where Z_1 and Z_2 are the front- and back-end impedance of the taper transmission line, respectively, and $\eta_v = 0.62$. The output voltage of the taper transmission line is approximately 0.6 MV, which is suitable for pumping a KrF laser.

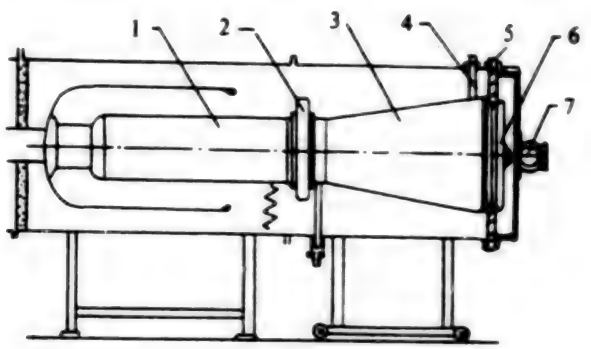


Figure 3. The Side View of the Blumlein Transmission Line Followed by a Taper Transmission Line

1. Blumlein transmission line; 2. prepulse switch; 3. taper transmission line; 4. resistance divider; 5. current shunt; 6. diode; 7. laser oscillator

Before experimenting with a diode, a 2.5Ω load was placed behind the taper transmission line to measure its voltage efficiency. Table 3 shows that the experimental data agrees well with calculated values.

Table 3. The Experimental Values of the Voltage Efficiency of the Taper Transmission Line

charging V. of M – generator (MV)	firing V. of main switch (MV)	V. at the front of TT – line (MV)	V. at the end of TT – line (MV)	V. efficiency of TT – line	
				Exp. value (%)	Cal. value (%)
1.0	0.79	0.78	0.47	60	62
0.8	0.64	0.63	0.38	61	62

The use of a taper transmission line with a pre-pulse switch between the Blumlein transmission line and the taper transmission line has two advantages. One is that the pre-pulse amplitude is reduced by a factor of 100. The pre-pulse is less than 1 kV in amplitude. The other is that the rise times of the voltage and current waveforms become faster.

Figure 4 [photograph not reproduced] shows that the rise time decreases after the pressure of the pulse switch is increased.

III. Production of Unpinched Intense E-Beam

The cathode of the diode is rectangular in shape; it can be 8 x 38 cm, 7.6 x 46.6 cm (diode impedance 6-9Ω) or 12 x 75 cm (diode impedance 2.5-4Ω) in size. The electrode gap ranges from 1.8 to 2.8 cm. A carbon felt should be evenly spread across the cathode surface. The cathode should have very good contact with its support structure. The edges of the rectangular cathode support structure must be well polished to avoid arc formation with ground or the cathode. The pressure inside the diode should be below 10^{-3} torr to prevent the neutralization of space-charge electrons by background gas ionization.

In our experiments, multi-point cathode, graphite cathode, brush cathode and carbon felt cathode were used. Our results indicate that a carbon felt cathode produces a more uniform e-beam. Furthermore, it takes less time, approximately 10 ns, to reach the space-charge-limited current. At a current density of 250 A/cm^2, we studied four anode coatings (i.e., 25 μm Ti, 50 μm Al, carbon- or aluminum-coated 50 μm Kapton film). Our results show that 25 μm Ti and 50 μm Al have longer life.

The space-charge-limited current density in a parallel plate diode can be expressed as follows:

$$J = 2340\ V^{3/2}X^{-2} \qquad (1)$$

Here, X is the electrode gap. When the unit of V is MV, the unit of X is cm and the unit of current density is A/cm^2. Figure 5 shows the current and voltage waveforms when the gap spacing is 2.2 cm. When the Marx generator is charged to 1.2 MV, the e-beam energy is 6.3 kJ.

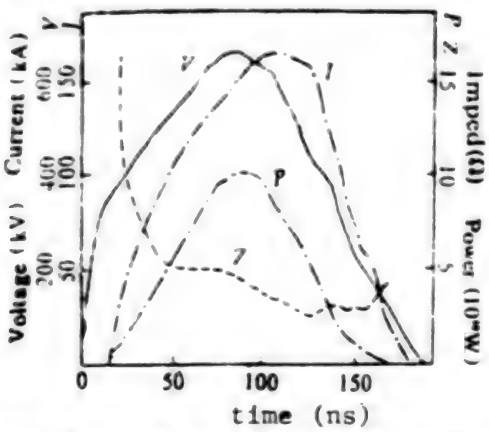


Figure 5. The Diode Current and Voltage Waveforms When Gap Spacing Was 2.2 cm

A key issue concerning the use of an e-beam to pump the laser is the current uniformity on the anode film. This is required for the uniform stimulation of the lasing medium. Moreover, the uniformity of current also affects the useful life of the anode film. Figure 6 shows the magnetic field associated with the rectangular e-beam.

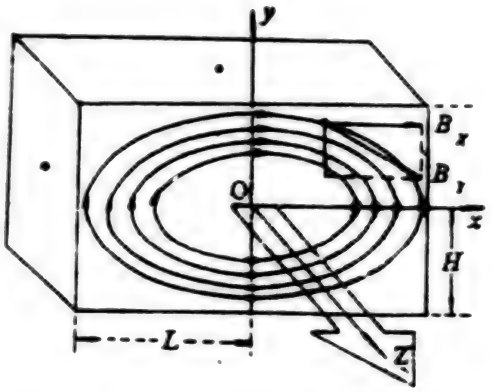


Figure 6. The Schematic Geometry of the Rectangular e-Beam and Its Magnetic Field

Figures 7 and 8 show the calculated self-magnetic fields of a 12 x 75 cm e-beam.[6]

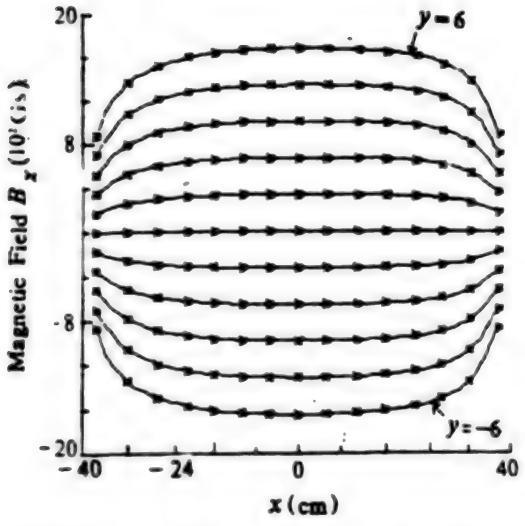


Figure 7. The Variation of Self-Magnetic Field B_x Along the Long Edge x of Beam When J Equals 220 A/cm^2; these curves represent 11 different y values
(y = 6, 4.8, 3.6, 2.4, 1.2, 0, ···, -6cm)

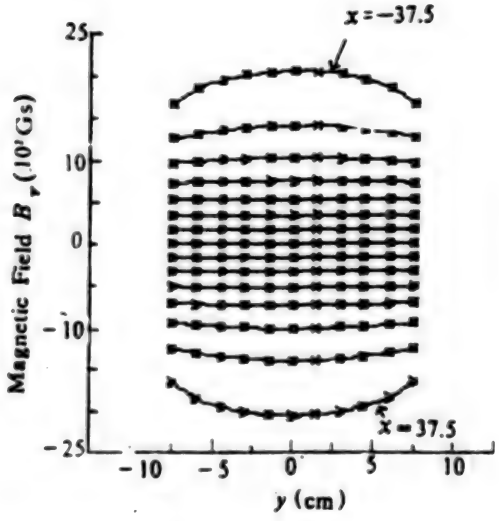


Figure 8. The Variation of Self-Magnetic Field B_y Along the Short Edge y of Beam When J Equals 220 A/cm^2; these curves represent 15 different x values
(x = 37.5, 32.14, 26.79, ···, 0, ···, -37.5cm)

The self-magnetic equation derived by Louis A. Rosocha of Los Alamos[7] can be expressed by equations (2) and (3). Assuming that the rectangular e-beam is 2L in length and 2H in width, its self-magnetic field can be expressed as:

$$B_x(x,y) = \frac{\mu_0 J}{4\pi}\{(x-L)\ln[\frac{(x-L)^2+(y-H)^2}{(x-L)^2+(y+H)^2}] - (x+L)\ln[\frac{(x+L)^2+(y-H)^2}{(x+L)^2+(y+H)^2}] + 2(y-H)[\tan^{-1}(\frac{x-L}{y-H}) - \tan^{-1}(\frac{x+L}{y-H})] - 2(y+H)[\tan^{-1}(\frac{x-L}{y+H}) - \tan^{-1}(\frac{x+L}{y+H})]\} \quad (2)$$

$$B_y(x,y) = -\frac{\mu_0 J}{4\pi}\{(y-H)\ln[\frac{(y-H)^2+(x-L)^2}{(y-H)^2+(x+L)^2}] - (y+H)\ln[\frac{(y+H)^2+(x-L)^2}{(y+H)^2+(x+L)^2}] - 2(x-L)[\tan^{-1}(\frac{y-H}{x-L}) - \tan^{-1}(\frac{y+H}{x-L})] - 2(x+L)[\tan^{-1}(\frac{y-H}{x+L}) - \tan^{-1}(\frac{y+H}{x+L})]\} \quad (3)$$

Our computation agrees with the results obtained with Rosocha's formula.

The self-magnetic fields at (0,H) and (L,0), two important positions causing beam pinching, can be written as:

$$\begin{cases} B_x(0,H) = \frac{\mu_0 J}{4\pi}\{-2L\ln\frac{L^2}{L^2+4H^2} + 8H\tan^{-1}\frac{L}{2H}\} \\ B_y(L,0) = -\frac{\mu_0 J}{4\pi}\{-2H\ln\frac{H^2}{H^2+4L^2} + 8L\tan^{-1}\frac{H}{2L}\} \end{cases} \quad (4)$$

When L = mH (m is a multiple)

$$\frac{B_x(0,H)}{B_y(L,0)} = \frac{-m\ln\frac{m^2}{m^2+4} + 4\tan^{-1}\frac{m}{2}}{-\ln\frac{1}{1+4m^2} + 4m\tan^{-1}\frac{1}{2m}} \quad (5)$$

In order to analyze the effect of the self-magnetic field on e-beam pinching, let us discuss a special case, i.e., w/l >> 1 (l is the length, l = 2L; w is the width, w = 2H).

At the center across its length of the rectangle (x = 0, y = ± w/2), the self-magnetic field only has an x component:

$$B_x = \frac{\mu_0 I}{2l} \quad \text{when } y = +\frac{w}{2} \quad (6)$$

$$B_x = -\frac{\mu_0 I}{2l} \quad \text{when } y = -\frac{w}{2} \quad (7)$$

At the center across its width (y = 0, x = ± l/2), the self-magnetic field only has a y component:

$$B_y = -\frac{\mu_0 I}{2\pi l}\left[1 + \ln\left(\frac{2l}{w}\right)\right] \quad \text{when} \quad x = \frac{l}{2} \tag{8}$$

$$B_y = \frac{\mu_0 I}{2\pi}\left[1 + \ln\left(\frac{2l}{w}\right)\right] \quad \text{when} \quad x = -\frac{l}{2} \tag{9}$$

Here, I is the e-beam current.

The critical current can be expressed as[8]

$$I_c = 2700\beta\gamma\frac{l}{d} \qquad \text{(long side)} \tag{10}$$

$$I_c = \frac{8500\beta\gamma}{1 + \ln\left(\frac{2l}{w}\right)}\frac{l}{d} \qquad \text{(short side)} \tag{11}$$

When $1/w \approx 6$, $l \times w \approx 900$ cm^2 and diode voltage V_d = 600 kV, the variations of diode impedance and I/I_c ratio with electrode gap are as shown in Table 4.

Table 4. The Variations in the Impedance and Critical Current Ratio With Electrodes Spacing

d (cm)	1.5	1.8	2.1	2.4	2.7
Z (Ω)	1.38	1.99	2.71	3.53	4.47
$\frac{I}{I_c}$ (short edge)	1.87	1.56	1.33	1.17	1.03
$\frac{I}{I_c}$ (long edge)	1.66	1.38	1.19	1.04	0.92

Hence, we can reach an important conclusion. It requires several diodes to yield a uniform intense e-beam and it must have a guiding magnetic field as well. From Table 4, I/I_c increases as impedance falls. Therefore, self-pinching is almost unavoidable. We need to have a multiple of separated diodes to provide a large current.

IV. Laser Oscillator and Laser Energy Output

Figure 9 shows a schematic diagram of the laser oscillator experiment. The peak voltage of the diode is 0.58 MV, peak current is 155 kA and half width (FWHM) of the current waveform is 100 ns. The laser cavity length is 90 cm; the stimulation zone is 75 cm long and 20 cm in diameter with a volume of 23.6 L. The cavity window is made of quartz. The interface between the window and the gaseous lasing medium is coated with an anti-reflective coating. The window is at a 15° angle with respect to the direction normal to the laser axis. This angle of inclination is chosen to minimize the background light caused by window reflection. The reflectance of the reflective mirror is 0.98 and the reflectance of the coupler is 0.3. The gas mixture in the cavity is 10 percent Kr, 0.4 percent F_2 and 89.6 percent Ar. The pressure is adjustable between 1 and 3.5 atm.

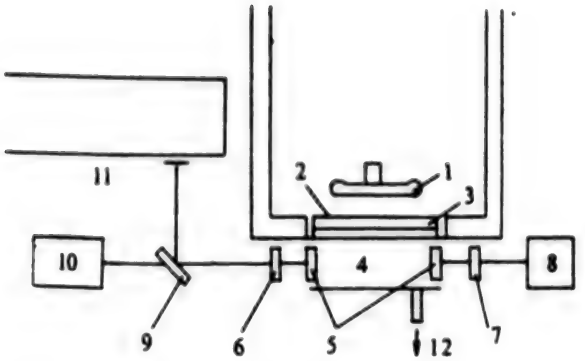


Figure 9. The Arrangement for the KrF Laser Experiment

1. cathode; 2. anode; 3. HIBACHI-type assembly; 4. laser cell; 5. cell windows; 6. output coupler; 7. total reflector; 8. photodiode; 9. splitter; 10. calorimeter; 11. plane grating spectrograph; 12. vacuum and gas system

Because the calorimeter is 10 cm in diameter, the laser beam emitted from the 20-cm-diameter coupler must be shrunk to below 10 cm with lenses before its energy can be measured with the SCIENPECH 38-8UV5 calorimeter. The time profile of the laser is measured by two GD-51 photodiodes. The rise time of the photodiode is less than 1 ns. The laser waveform is similar to that of the e-beam, but a bit narrower, as shown in Figure 10. The fluorescence waveform is essentially consistent with the e-beam waveform.

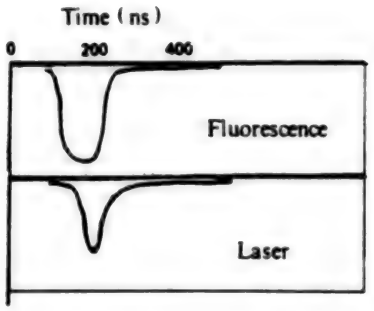


Figure 10. Time-Correlated Laser Medium Spontaneous Emission and Laser Output

Figures 11 and 12 show the laser spectrum and fluorescent spectrum measured by the 2 m plane grating spectrograph. They were analyzed by a 3CS micro-densitometer. Limited by the sensitivity of the spectrograph, the fluorescent spectrum was only measured in the vicinity of 248 nm.

In order to study the dependence of laser power output as a function of e-beam pumping power, a model was established to describe e-beam energy deposition and KrF laser kinetics.

$$\frac{\partial \Phi_\pm}{\partial t} \pm C \frac{\partial \Phi_\pm}{\partial x} = C\left(\frac{g_0 - \alpha_0}{1 + (\Phi_+ + \Phi_-)/\Phi_s} - \alpha_s \right)\Phi_\pm \qquad (12)$$

Here, Φ_+ (Φ_-) is the light flux along positive (negative) x-axis, $\Phi_s = h\nu/\sigma\tau_1$ is the saturated light flux, g_0 is the small-signal gain, and α_0 and α_n are the saturated and unsaturated absorption coefficients, respectively.

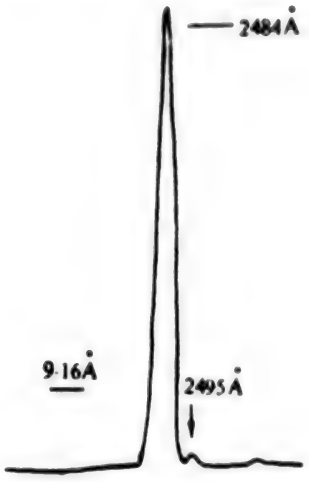


Figure 11. Laser Spectrum of KrF (89.6 percent Ar, 10 percent Kr, 0.4 percent F at 2 atm)

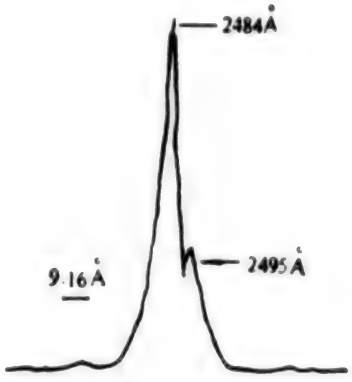


Figure 12. Fluorescence Spectrum of KrF (89.6 percent Ar, 10 percent Kr, 0.4 percent F at 2 atm)

α_0 and g_0 have identical saturated light flux. The absorption by F_2, F^-, Kr_2 and Ar_2 is of unsaturated nature. The absorption of Kr_2F^* is of saturated nature because KrF^* is the precursor of Kr_2F^*. It is the same as the saturated flux of laser transition.

Integrating equation (12) with respect to x, we get the differential equation of laser flux with respect to time.

$$\frac{d\langle \Phi_c \rangle}{dt} = C\left(\frac{g_0 - \alpha_0}{1 + \langle \Phi_c \rangle / \Phi_s} - g_c - \alpha_n \right) \langle \Phi_c \rangle \tag{13}$$

Here, $\langle \phi_c \rangle$ is the spatial mean flux and g_c is the cavity loss.

$$g_c = -\frac{1}{2L} \ln (R_a R_b) \tag{14}$$

R_a and R_b are the effective reflectance values of both ends of the optical cavity from the viewpoint of the stimulation zone.

$$R_a = (T_{F_1} \; T_{w_1})^2 R_1 \tag{15}$$

$$R_b = (T_{F_2} \; T_{w_2})^2 R_2 \tag{16}$$

Here, T_{F1} is the penetration rate in the non-pumping zone F_1 between x = 0 and window 1, T_{F2} is the penetration rate in the non-pumping zone F_2 between

x = L and window 2; T_{W1} and T_{W2} are the transmittance values of windows 1 and 2, respectively. The definitions of these parameters are shown in Figure 13.

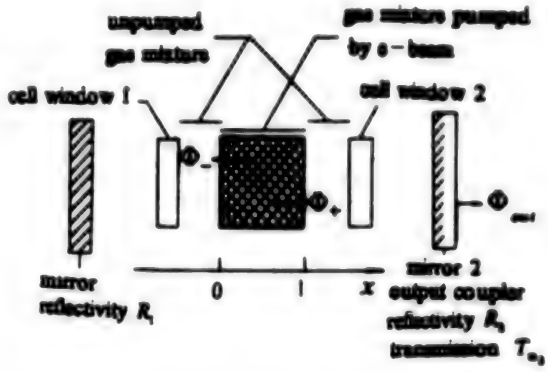


Figure 13. Schematic Representation of the KrF Oscillator Configuration

The laser flux coming out of the cavity is:

$$\Phi_{out} = \frac{(1-R_2)T_{F_2} \cdot T_{W_2}}{1+R_2(T_{F_2} \cdot T_{W_1} \cdot T_{F_1} \cdot T_{W_2})^2} \langle \Phi_C \rangle \tag{17}$$

The energy from the cavity is

$$E = \int_T \Phi_{out} \cdot S \cdot h\nu \, dt \tag{18}$$

Here, S is the area of the laser cavity window and hν = 5 eV.

The energy deposition rate of the e-beam in the laser cavity is

$$\varepsilon_d = S_{Ar} \cdot I_{Ar} + S_{Ar^*} \cdot I_{Ar^*} + S_{Kr} \cdot I_{Kr} + S_{Kr^*} \cdot I_{Kr^*} \tag{19}$$

Here, S represents the rate of ionization or excitation between electron and a certain ★ species and $I_★$ represents the mean ionization energy or excitation energy between electron and species ★.

The energy pumped into the cavity by the e-beam is

$$E_d = \int_V \int_T \varepsilon_d \, dt \, dV \tag{20}$$

Here, V is the stimulation volume and T is the pulse width of the e-beam.

Let us define the intrinsic efficiency of the laser oscillator as the ratio of laser energy to energy deposited in the gas:

$$\eta = \frac{E}{E_{\cdot}} = \frac{\int_T \Phi_{out} Sh\nu dt}{\int_V \int_T \varepsilon_i dV dt} \tag{21}$$

In Figure 14, we calculated intrinsic efficiency versus e-beam current density curves for three different laser oscillators. The composition of the gas mixture remains constant at Ar: 89.6 percent, Kr: 10 percent, F_2: 0.4 percent.

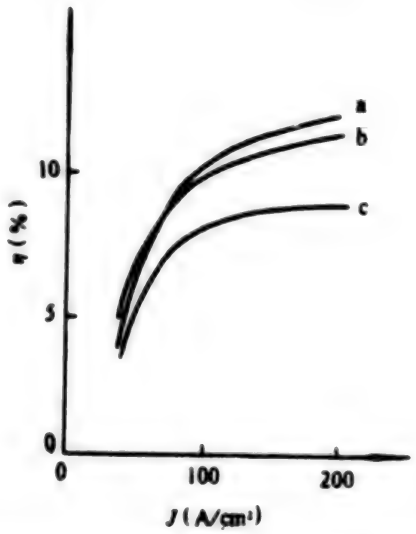


Figure 14. Theoretical Calculation of the Dependence of the Intrinsic Efficiency η on the Beam Density

1. Φ70mm. L = 38cm. p = 2280Torr. R_1 = 30%
2. Φ110mm. L = 60cm. p = 2280Torr. R_1 = 30%
3. Φ200mm. L = 75cm. p = 1900Torr. R_1 = 30%

The calculation shows that the intrinsic efficiency η = 8 percent when the current density J = 200 A/cm^2. This is consistent with experimental results. In the experiment, the e-beam energy is approximately 5 kJ, e-beam film penetration and transport efficiency is 50 percent, and electron energy deposition in gas is about 50 percent. Based on an 8 percent intrinsic efficiency, the output energy is around 100 J. This is very close to the calculated value of 106 J.

References

1. Wang Naiyan, Zeng Naigong et al., Proc. of 5th Inter. Top. Conf. on High Power Electron and Ion Beam Research and Tech., p 60 (1983), San Francisco.

2. Wang Naiyan et al., "Particle Beam Fusion Research at IAE in Beijing," LASER AND PARTICLE BEAMS, 5 (1), 89-99 (1987).

3. Wang Ganchang, Zhu Xuhui, Wang Naiyan, Xie Jinggang, Li Yingshan, Zhou Changhuai and Wang Pu, "The Generation of 6 J KrF Laser System," NUCL. SCI. AND ENG., 5 (1), (1985).

4. Wang Ganchang, Zhu Xuhui, Wang Naiyan, Xie Jinggang, Li Yingshan, Zhou Changhuai and Wang Pu, "Studies of KrF Laser Pumped by an Intense Relativistic Beam."

5. Wang Ganchang, Zhu Xuhui, Wang Naiyan, Xie Jinggang, Li Yingshan, Zhou Changhuai and Wang Pu, "12.5 J KrF Excimer Laser Pumped by a High-Intense Relativistic Electron Beam," APPL. OPT., 6 (2), 49 (1986).

6. Gao Junsi, Wang Naiyan, "A Self-Magnetic Field Calculation for a Rectangular High-Current Electron Beam," IAE Report -- 1990, Beijing.

7. Louis A. Rosocha and Kenneth Bruce Riepe, FUSION TECHNOLOGY, 11, May, 576 (1987).

8. M. Rokni, J. H. Jacob and J. A. Mangano, PHYS. REV., A 16, 2216 (1977).

Kinetic Simulation of KrF Laser

92FE0307B Chengdu QIANG JIGUANG YU LIZI SHU [HIGH POWER LASER AND PARTICLE BEAMS] in Chinese Vol 3 No 4, Nov 91 pp 457-463

[Article by Kang Xiangdong [1660 0686 2639], Shan Yusheng [0830 3768 3932], and Wang Naiyan [3769 0035 1750] of China IAE, Beijing: "Kinetic Simulation of KrF Laser"; MS received 6 Nov 89, revised 10 Jan 91]

[Text] Abstract

A zero-dimensional simulation of the kinetics of KrF laser is done as a part of the design work. The results are compared with experimental data reported worldwide. A simple and practical model is introduced to improve the intrinsic efficiency of KrF laser, determine the requirements for the incident e-beam, and provide excellent recommendations for the design of the laser cavity.

Key Words: KrF laser, KrF laser kinetics.

I. Introduction

The KrF laser is one of the most promising devices for inertial confinement fusion (ICF). The kinetics of KrF laser is one of the most important subjects to study in the development of KrF lasers. By way of simulation, the KrF laser can be optimized[1] and the effect of various parameters can be analyzed. As far as simulation is concerned, a relatively simple method is a zero-dimensional simulation which assumes the KrF cavity contains a uniform active agent.[2,3] However, in order to solve more delicate problems such as relaxation vibration and amplified spontaneous emission (ASE), a one-dimensional simulation along the optical axis is more appropriate.[1,4]

In coordination with the development of the 100 J KrF laser at IAE, we conducted a simulation study on the kinetics of the KrF laser to provide some bases for improving the intrinsic efficiency of the laser, determining the requirements for the incident e-beam, and optimizing the design of the laser cavity. This can also provide some guidance to the selection of the optimal gas mixture composition and optimal output coupling in our experimental work.

The second section describes the simulation of the lasing process. The third section compares calculated results with available experimental data. Some requirements for the e-beam are also presented based on simulation.

II. Simulation

The higher energy state of the KrF laser is achieved by pumping a gas mixture (Ar, Kr, F_2) with an e-beam in a cavity. This is followed by spontaneous emission along the optical axis to produce laser oscillation. (It can also be used as an amplifier by injecting a laser into it to produce laser amplification.) Figure 1 is a schematic showing the principle of a KrF laser.

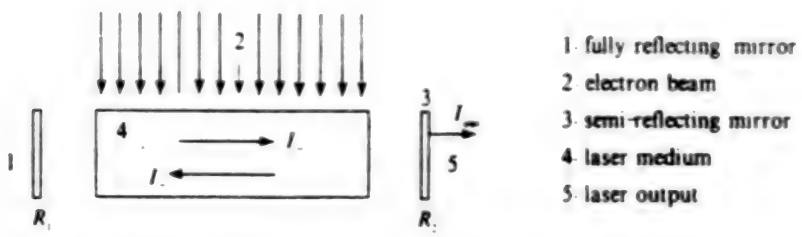


Figure 1. Diagram of KrF Laser Facility

The overall framework to simulate the process from e-beam pumping, through KrF excimer production, to laser output is as follows:



1. Energy Deposition (Pumping Rate) of Incident E-Beam in Laser Cavity

When an intense relativistic e-beam is injected into a laser cavity filled with Ar, Kr and F_2, because the F_2 content is very low (0.4 percent), most of the e-beam energy pumps into Ar and Kr to cause the ionization and excitation of these atoms.

$$e + \begin{cases} \begin{pmatrix} Ar \\ Kr \end{pmatrix} \longrightarrow \begin{pmatrix} Ar^{+} \\ Kr^{+} \end{pmatrix} + e + e_s \\ \begin{pmatrix} Ar \\ Kr \end{pmatrix} \longrightarrow \begin{pmatrix} Ar^{*} \\ Kr^{*} \end{pmatrix} + e \end{cases} \qquad (1)$$

Here, e is the beam electron and e_s is the secondary electron. The pumping of e-beam energy into a laser cavity is a relatively complicated process. A detailed method is to calculate it by using a special MC (Monte Carlo) simulation program. There is also another simple method[5] which involves the use of a modified cross section of reaction (1) in the simulation. This modification takes the diffusion of electrons in the gas mixture into account by simulation. This modified cross section is used in this work.

Let S be the rate for a particular species of particle to generate electron ionization or excitation per unit volume and I be the average ionization or excitation energy of that particle, then the e-beam pumping power ε_d is written as follows:

$$\varepsilon_d = S_{Ar} \cdot I_{Ar} + S_{Ar^*} \cdot I_{Ar^*} + S_{Kr} \cdot I_{Kr} + S_{Kr^*} \cdot I_{Kr^*}$$

Thus, the energy pumped E_d is

$$\int_t \int_{T_0} \varepsilon_d dt dV$$

Here, V is the active volume and T_0 is the duration of the pulse.

2. Formation and Dissipation of KrF^* and Laser Output

The KrF laser is generated by e-beam stimulation, a process whose major steps are shown in Figure 2. The reaction cross section for each step can essentially be found in reference 5.

For every substance listed in Figure 2, a rate equation can be established:

$$\frac{dN_i}{dt} = \sum F_i - \sum_i D_i \qquad (i = 1, 2, 3, \cdots, m) \qquad (2)$$

where N_I is the density of a certain particle, F and D are the formation and dissipation terms, respectively. For instance, with respect to a reaction such as A + B → C + D, the formation term for particle C (or D) is

$$F = f_{xy}[A] \cdot [B]$$

Here, [x] or [y] is the particle density of substance x or y, and f_{xy} is the reaction rate constant. For particle A (or B), the dissipation term is

$$D = k_{xy}[A] \cdot [B]$$

(k_{xy} is the dissipation reaction rate.)

The light intensity I inside the laser cavity is taken into account using a zero-dimensional model. Then, the laser equation becomes:

$$\frac{1}{c} \frac{dI}{dt} = I(g - g_a - g_m) \qquad (3)$$

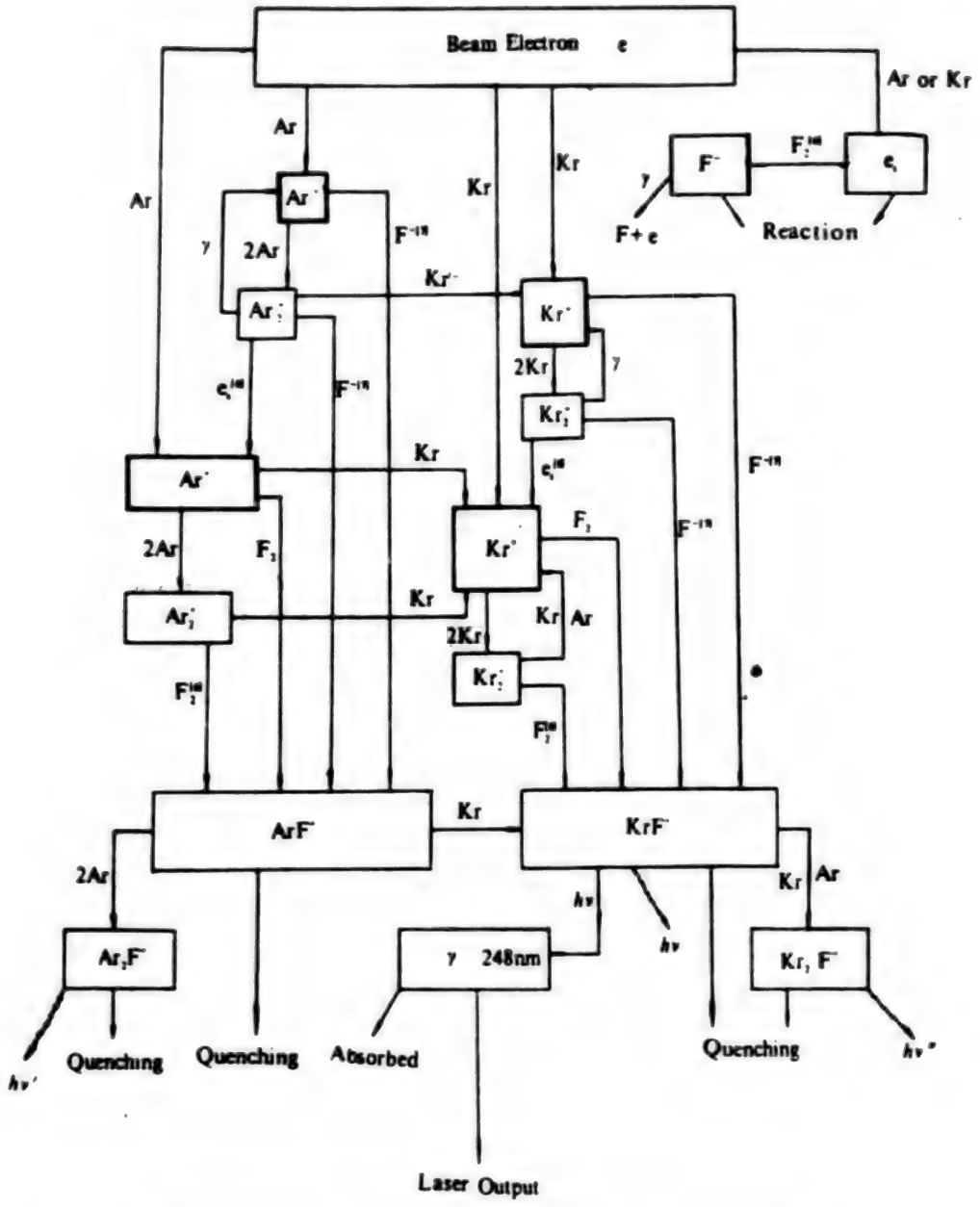


Figure 2. Schematic of Generation of KrF

Here, g_α is the light absorption term:

$$g_\alpha = f_{F^-,\gamma}[F^-] + f_{F_2,\gamma}[F_2] + f_{Ar_2^*,\gamma}[Ar_2^*] + f_{Kr_2^*,\gamma}[Kr_2^*] + f_{\underbrace{\quad}} [Kr_2F^*] + f_{Ar_2F^*,\gamma}[Ar_2F^*]$$

[indistinguishable]

where g is the stimulated emission term (gain factor):

$$g = \sigma_{st} \cdot [KrF^*].$$

g_{th} is the threshold for laser oscillation:

$$g_{th} = -\frac{1}{2L} \ln(R_1 \cdot R_2)$$

σ_{st} is the stimulated emission cross section, R_1 and R_2 are the reflectance values of the two mirrors of the resonance cavity (R_1 is the reflective mirror and R_2 is the output mirror), and L is the length of the active material.

In reality, there should be another transient term on the right side of the equation, i.e., the spontaneous radiation in the direction of the optical axis. This term triggers laser oscillation initially. However, it becomes too small to appear in the laser equation.

Based on equations (2) and (3) and the reaction path shown in Figure 2, a series of rate equations describing the generation of the KrF^* laser can be established. This is a series of first-order differential equations. They can be solved by the fourth-order Runge-Kutta method. Thus, the formation of a KrF laser can be simulated.

$$e + \begin{pmatrix} Ar_2^+ \\ Kr_2^+ \end{pmatrix} \rightarrow \begin{pmatrix} Ar^* \\ Kr^* \end{pmatrix} + \begin{pmatrix} Ar \\ Kr \end{pmatrix}$$

The rate constant for the above equation is a function of electron temperature T_e and room temperature T:[6]

$$f_{Ar_2^+ e} = 7.5^{-7} \left(\frac{T_e}{T}\right)^{-0.67} (cm^3/s)$$

$$f_{Kr_2^+ e} = 1.2^{-6} \left(\frac{T_e}{T}\right)^{-0.5} (cm^3/s)$$

In the laser formation process, the rates of combination between F^- and Ar^+, Ar_2^+, Kr^+ and Kr_2^+ are dependent upon the background Ar pressure. The rate constants are usually determined from experimental curves.[7]

For the laser cavity shown in Figure 1, usually $R_1 = 1$ for the reflective mirror. The laser output intensity I_{out} is

$$I_{out} = \frac{1 - R_2}{1 + R_2} \cdot I$$

The total laser energy output E is:

$$E = \int I_{out} Sh\nu dt$$

where S is the window area and $h\nu = 5$ eV is the photon energy.

The intrinsic efficiency of the laser η is:

$$\eta = \frac{E}{E_d}$$

where E_d is the pumped e-beam energy.

III. Results and Discussion

Calculations were made for experiments performed at IAE in 1985 and 1986,[9,10] as well as for work done at Sandia.[8] A comparison is shown in Table 1.

Table 1

	IAE Lab (1985)		IAE Lab (1986)		Sandia Lab	
	Experiment	simulation	Experiment	simulation	Experiment	simulation
laser output	12.5J	16J	19.4J	23J	80J	82J
intrinsic laser efficency		8.8%		9.1%	10%	11.4%
laser output power		8.1MW/cm^2		7.8MW/cm^2	30MW/cm^2	31.4MW/cm^2
pump rate of input laser cavity		1.9MW/cm^3		1.9MW/cm^3	7MW/cm^3	7MW/cm^3

In addition, Figure 3 graphically compares calculated results to Sandia's experimental data (current, laser and sidelight). The beam current used for simulation is shown as the dotted curve in Figure 3. When the pumping power is comparable to that used experimentally by Sandia, the computation is essentially in agreement with the experimental data. Since the work done at IAE involved single-pulse experiments, a typical experimental current level is used in the simulation. There is good agreement between calculated and experimental results as well. We must stress that the beam current used at IAE in 1985 is essentially the same as that used in 1986. However, the pulse width used in 1985 is 30 ns narrower compared to that used in 1986. Both experimental and calculated results show that wider current pulses are better for high energy laser output.

In this modeling work, we also varied the beam current to calculate the lasing process of three laser cavities; (a) laser cavity output aperture ϕ = 7 cm, active length L = 38 cm, total pressure p = 2280 Torr, output mirror reflectance R_2 = 30 percent; (b) ϕ = 11 cm, L = 60 cm, p = 2280 Torr, R_2 = 30 percent; (c) ϕ = 20 cm, L = 75 cm, p = 1900 Torr, R_2 = 20 percent under typical conditions (pressure ratio Ar/Kr/F_2 = 89.6%/10%/0.4%). Figure 4 shows the curve for simulated intrinsic laser efficiency η versus current density J. One can see that η increases rapidly with J in the low current density zone (J < 100 A/cm^2). After J reaches 100 A/cm^2, η approaches a constant value. Obviously, there is considerable advantage in adjusting the beam current density to above 100 A/cm^2, which also facilitates high energy laser output.

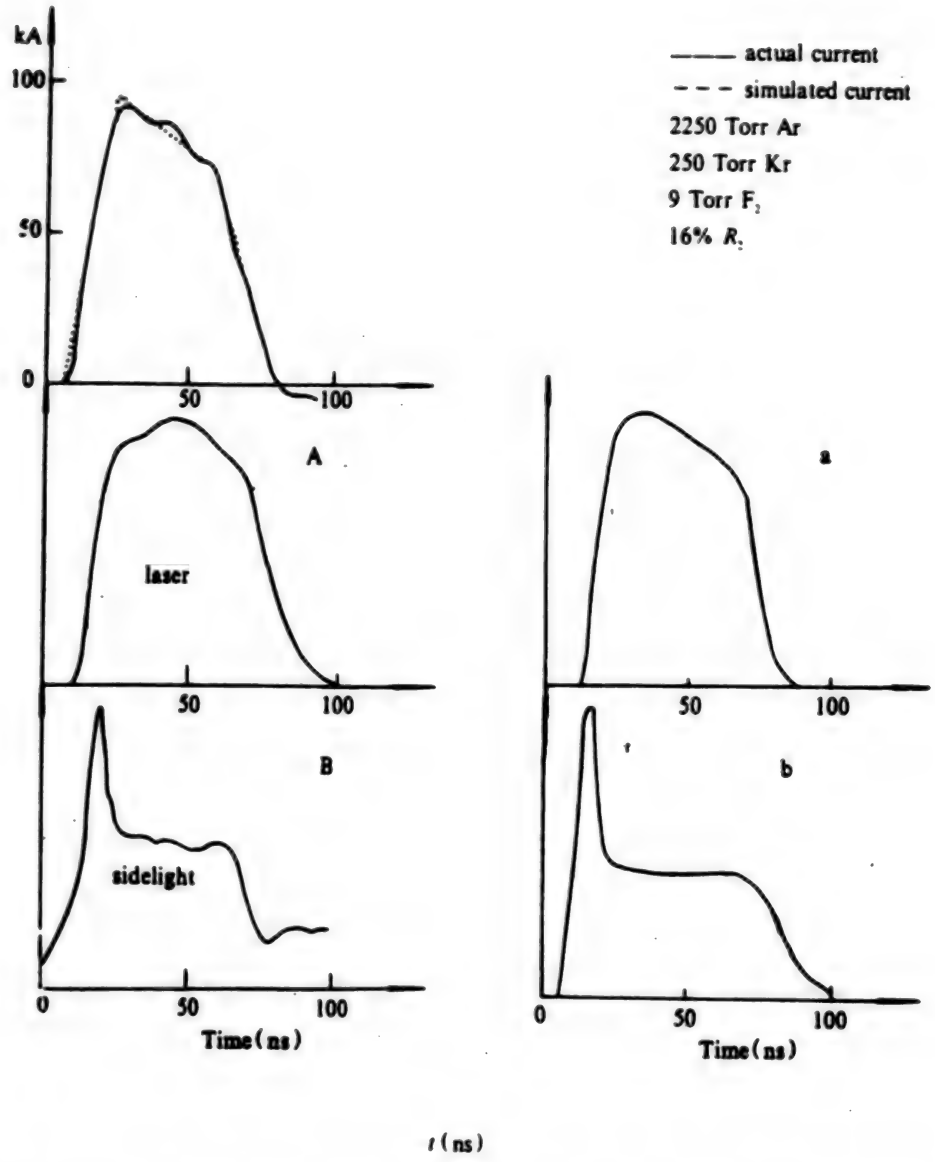


Figure 3. Comparison Between Simulation and Sandia Experiment Results. A, B experiment value; a, b simulation

Our calculation shows that in a 75-cm-long cavity with a 20 cm output aperture (which is confirmed to be a 100 J KrF laser cavity), assuming the pulse width is 70 ns, the pumping power of the e-beam reaches 1.5 MW/cm^3. This means that the laser output could reach 100 J. This result was experimentally confirmed.[11]

Furthermore, the total laser energy output was calculated as a function of current rise time. The results indicate that the rise time does not play a critical role in the design of the cavity. Of course, when factors such as the physical characteristics of the accelerator are taken into account, current rise time does affect the power output of the e-beam.

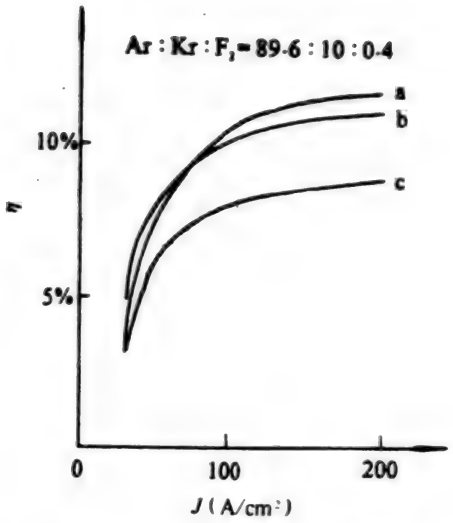


Figure 4. Simulation for Intrinsic Efficiency η Versus Density J of Beam Current
a. ϕ = 7 cm, L = 38 cm, p = 2280 Torr, R_2 = 30%
b. ϕ = 11 cm, L = 60 cm, p = 2280 Torr, R_2 = 30%
c. ϕ = 20 cm, L = 75 cm, p = 1900 Torr, R_2 = 20%

Based on the results discussed so far, we believe that with the existing accelerator at IAE, in addition to enlarging the aperture, volume and active material of the laser cavity, we must raise the beam current density to above 100 A/cm^2. Furthermore, after this condition is met, the current pulse needs to be widened to the extent possible.

As we go on further, the program can be used to obtain the optimal coupling for the output mirror. Furthermore, it can be used to optimize parameters such as gas composition and total pressure. Preliminary results indicate that the reflectance of the output mirror needs to be lowered to improve the laser efficiency as the performance of the accelerator is upgraded and the e-beam pumping rate is raised. Since the simulation program is relatively simple, it enables us to quickly understand laser formation processes under different operating conditions. Then, various parameters associated with the KrF laser can be analyzed. This simplicity and applicability of the program have been illustrated. In order to further perfect the program, a more detailed study on excimer lasers is required. We are now considering some one-dimensional simulation on this topic.

References

1. Stephen J. Czuchlewski, et al., FUSION TECHNOLOGY, 11, May, 560 (1987).

2. Thomas H. Johnson, et al., IEEE J. QUANTUM ELECTRON, QE-15,289 (1979).

3. W. J. Witteman and B. M. H. H. Kleikamp, J. APPL. PHYS, 55 (5), 1299 (1984).

4. Fumihiko Kannari, et al., J. APPL. PHYS., 57 (9), 4309 (1985).

5. Thomas H. Johnson and Allen M. Hunter, J. APPL. PHYS., 51 (5), 2406 (1980).

6. "Excimer Laser," Edited by Ch. K. Rhodes.

7. J. M. Waderha and J. N. Bardsley, APPL. PHYS. LETTERS, 32, 76 (1978).

8. James K. Rice, et al., IEEE J. QUANTUM ELECTRON. QE-16,1315 (1980).

9. Wang Ganchang [3769 3227 2490], et al., YINGYONG JIGUANG [APPLIED LASER TECHNOLOGY], Vol 6, 1986, p 49.

10. Wang Naiyan, Zhou Chuangzhi [0791 0482 1807], et al., Internal Report of the China IAE, 1987.

Multi-Electron-Beam Cerenkov FEL Oscillator

92FE0307C Chengdu QIANG JIGUANG YU LIZI SHU [HIGH POWER LASER AND PARTICLE BEAMS] in Chinese Vol 3 No 4, Nov 91 pp 445-449

[Article by Wang Qingyuan [3769 3237 3293], Yu Shanfu [0060 0810 1133], Xun Peijue [1416 1014 3778], and Liu Shenggang [0491 4141 4854] of the University of Electronic Science and Technology of China and He Kesong [5170 0344 2646], Chen Yutao [7115 5940 3447], and Wang Pingshan [3769 1627 1472] of China Academy of Engineering Physics (CAEP): "Multi-Electron-Beam Cerenkov FEL Oscillator"; MS received 5 Jan 91, revised 18 Jun 91]

[Text] Abstract

The multi-electron-beam Cerenkov FEL has been experimentally demonstrated for the first time. Electron beams with a total current of 280 A at 500 kV were introduced into a multi-dielectric rectangular cavity and 1.7 MW Cerenkov coherent stimulated radiation was generated at 33.4 GHz. The efficiency is 1.2 percent.

Key Words: multi-electron-beam Cerenkov FEL, oscillator, coherent stimulated emission.

I. Introduction

In areas such as communications, plasma heating and solid state physics, the need for a high-power, short-wavelength microwave source stimulates rapid progress in relativistic microwave electronics. The Cerenkov FEL is simple in structure and uses medium-energy electron beams. It has a great potential to become a widely used high-power, high-efficiency, continuously tunable centimeter-wave (i.e., far infrared) coherent stimulated emission source.

When the velocity of charged particles traveling at the surface of or in a dielectric exceeds the speed of light in that medium, Cerenkov spontaneous emission takes place.[1] In a dielectric waveguide, the interaction between this spontaneous emission with an electron beam (e-beam) can be converted into coherent stimulated emission. The frequency is determined by the synchronous condition between the e-beam velocity and the phase velocity of the waveguide mode.[2] Experimental studies on the Cerenkov FEL have been done in the past 20 years. In 1977, J. E. Walsh et al. obtained 1 MW output

at 30 GHz and 60 GHz by using a 10 kA relativistic electron beam at 500 kV.[3] Between 1981 and 1985, that group achieved 30-120 kW output power in the frequency range of 50-100 GHz using medium-energy e-beams (100-180 kV).[4-6] In 1989, William Main et al. produced centimeter waves at 3.8 GHz by using 12 kA, 700 kV relativistic e-beams and the output power reached 200 MW.[7] In the meantime, a great deal of progress has been made in experimental research on short-millimeter-wave, far-infrared, Cerenkov FEL.[8,9]

The Cerenkov FEL can generate high-power centimeter-wave, far-infrared stimulated emission, by using medium-energy (100-400 kV) electron beams generated by a conventional e-beam source. Compared to a conventional FEL which requires a cyclotron or undulator, its weight and volume can be effectively reduced to lower its cost. However, in a slow-wave device, e-beams interact with the "tail field" in the waveguide. If the beam path is not small enough, inhomogeneity of the longitudinal electric field component would drastically affect the quality of the e-beam. Consequently, the efficiency of the device is adversely affected. Experimentally, the e-beam path is approximately 7 mm at 50 GHz[5] and 2.5 mm at 100 GHz.[6] The current passing through the interaction zone is only around 10 A. The fact that the current path is too small, especially when the device operates in the far-infrared short-millimeter-wave region, is a direct cause affecting the power output because the beam current is limited.

In order to solve this problem, Wang Qingyuan et al. presented the concept of the multi-electron-beam Cerenkov FEL and conducted a theoretical analysis in 1989.[10] Ideally, if the slow-wave structure is completely filled with the dielectric waveguide, the electric field inside would not decay. However, the transport of e-beams in this waveguide would be very difficult. As a compromise, a multi-e-beam Cerenkov FEL has a multi-dielectric slow-wave structure. E-beams can travel in a number of channels between various dielectric layers to raise the beam current. The power capacity in the interaction zone can also be increased. With higher interaction efficiency ensured, the power output can also be significantly improved. The slow-wave system of a multi-e-beam Cerenkov FEL may be comprised of several concentric cylinders or several parallel dielectric plates. This paper reports the first experimental study of a Cerenkov FEL with the latter slow-wave structure.

II. Experimental Setup and Measured Results

Figure 1 shows the experimental setup for the multi-e-beam Cerenkov FEL. The 500 kV pulsed relativistic e-beams are supplied by the EPA-74 pulsed linear accelerator at CAEP. The cathode of the diode is a 15-mm-diameter hemispherical graphite emitter and the anode is a 96-mm-diameter non-magnetic stainless steel spherical crown. There is a 22-mm-diameter hole in the middle of the cathode. The spacing between the cathode and anode is 15 mm, a space which is exposed to the guiding magnetic field. The guiding magnetic field is generated by a solenoid on an 890-mm-long BJ-32 standard waveguide which can vary continuously between 0 and 10 kGs.

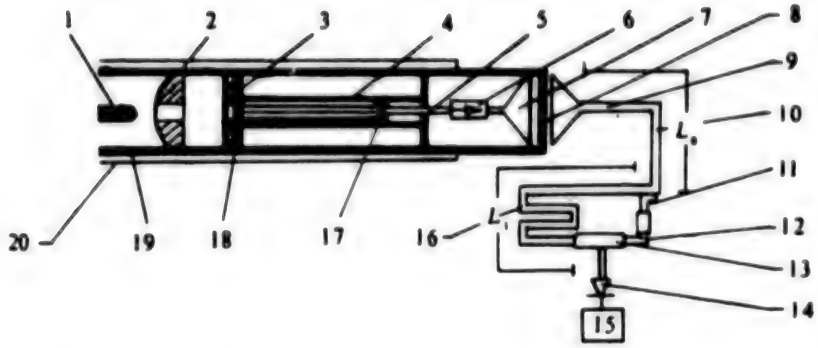


Figure 1. Schematic Diagram of the Apparatus for the Multi-Electron-Beam Oscillator Experiment

1. cathode; 2. anode; 3. beam-controlled plate; 4. slow-wave supporting system; 5. coupling waveguide; 6. isolator; 7. No. 1 standard horn; 8. window; 9. No. 2 standard horn; 10. standard transmission waveguide; 11. directed coupler; 12. attenuator; 13. double T; 14. crystal detector; 15. oscilloscope; 16. dispersive delay line; 17. second reflector; 18. iris; 19. BJ-32 waveguide; 20. solenoid

The multi-e-beam Cerenkov FEL oscillator is placed inside a sealed waveguide (i.e., BJ-32 standard waveguide). It consists of a beam control plate, iris, slow-wave system, rear reflector, coupling waveguide, isolator and 8 mm standard horn. The beam control plate has a 16-mm-diameter hole in the middle. The iris is a non-magnetic stainless steel plate with four 26-mm-long, 2-mm-wide slits. It ensures more electrons enter various beam paths without causing any damage to the dielectric plates. The slits are evenly spaced and the center-to-center distance is 4 mm. The beam control plate and iris also act as the front mirror for the resonant cavity. The slow-wave structure is comprised of the metal waveguide and five layers of 30-mm-wide, 97 percent ceramic plates ($\varepsilon = 10$). Each ceramic layer is evenly divided into five sections and each section is 89 mm long. Between two sections there is a 0.2-mm-thick stainless steel plate which stands out above the ceramic surface by 0.6 mm. It is used to absorb divergent electrons to protect the ceramic plates. Two 0.6-mm-thick ceramic layers adhere to the upper and lower surface of the metal waveguide, respectively (not illustrated in Figure 1). The remaining three layers are 1.2 mm thick. They are inserted in three slots on the waveguide wall which are spaced 4 mm apart. The last five sections are machined in wedge shape to minimize reflection of electromagnetic waves. The rear mirror has a 3.6 mm x 7.1 mm rectangular hole in the middle. The energy is transmitted outside the sealed waveguide through the coupling waveguide, isolator, 8 mm standard hole and a 5-mm-thick Plexiglass window.

The electromagnetic wave is received by another 8 mm standard horn outside the system. It is introduced into the testing hall by means of a 14-m-long, 8 mm standard transmission waveguide. It is divided into two beams by a 20 dB directional coupler. The main beam is sent to a double T input by way of a 57.2 m dispersive delay line. The branch beam goes through a variable

attenuator before entering the other input of the same double T connector. The output of the double T connector goes to a crystal detector. The signals are displayed on an oscilloscope (Model 7834). The frequency of the electromagnetic waves can be determined by measuring the time interval τ between two neighboring peaks.

$$f = \frac{f_c}{\sqrt{1-(L_1/c\tau)^2}} \tag{1}$$

where f_c is the cutoff frequency of the dispersive delay line, which is 21.1 GHz in this case; L_1 is the length of the dispersive delay line, which is 57.2 cm; and c is the speed of light. The second voltage signal V can provide us the total output power:

$$P = K\frac{V}{d}\,10^{\frac{\alpha(L_0+L_1)}{10}} \tag{2}$$

where K is the attenuation factor of the output window; d is the sensitivity of the crystal detector; L_0 is the length of the 8 mm standard transmission waveguide, which is 14 m; and α is the waveguide attenuation index.

First, we repeatedly tested the device using 500 kV electron beams with a 6 kGs guiding magnetic field. Figure 2 shows the typical diode voltage waveform. Figure 3 shows the typical radiation signals detected by the crystal detector and displayed on the Model 7834 oscilloscope. The time interval between two signals, τ, was determined to be 244 ns. From equation (1), the frequency of the microwaves generated is calculated to be 33.4 GHz. The voltage of the second signal is 150 mV. At this frequency, we found that α = 0.867, K = 4.85 and d = 1.25 mV/mW. From equation (2), the signal power is 1.7 MW.

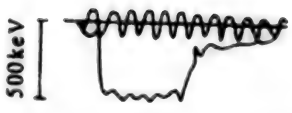


Figure 2. Typical Diode Voltage Signal

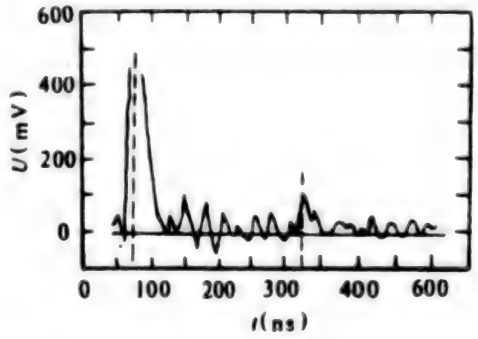


Figure 3. Typical Radiation Signals

We studied the effect of the guiding magnetic field on the operating frequency and power output with other parameters left unchanged. The results show that when the guiding magnetic field declines from 7.5 kGs to 4 kGs the operating frequency varies by less than 8 percent. Furthermore, it does not meet the increasing relation between frequency and the strength of guiding magnetic

field. This indicates that the signal is due to coherent stimulated Cerenkov emission. Nevertheless, the lowering of the guiding magnetic field causes the power output to fall. When the guiding magnetic field is below 3 kGs, the second voltage signal is buried in the noise.

The beam is measured with a 4.2Ω Faraday cup. The guiding magnetic field was maintained at 6 kGs. In order to measure the e-beam entering the front end of the interaction zone, the slow-wave system was taken out. The sealed waveguide only contains the beam control plate and iris, which remained in the same locations as described before. Figure 4 shows the measured beam waveform. The trailing waves are reflection caused by cable mismatch. The first wave shows a peak current of 350 A. In this case, each slit on the iris is 2 mm wide. In a slow-wave system, due to the presence of thin metal foils between dielectric plates, the slit width is only 1.6 mm. Therefore, the beam actually entering the interaction zone is only 80 percent of the measured value, i.e., 280 A. Based on the beam voltage, current and signal power, the efficiency of the oscillator is estimated to be 1.2 percent.

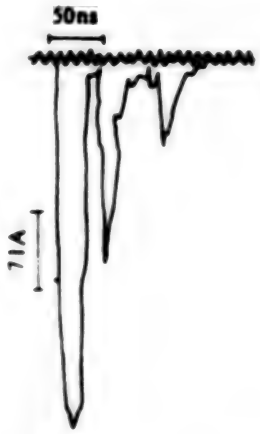


Figure 4. Measured Beam Current After the Iris

Due to beam divergence and deviation of beam movement direction from the oscillator axis, most electrons in the interaction zone collide with the metal absorber and fail to go across the region. With a slow-wave system and keeping identical parameters, the current measured at the rear end of the interaction zone is only 12 A. This problem can be solved more satisfactorily by properly adjusting the position of the slow-wave system.

III. Conclusions and Discussion

This paper reports the first experimental study of a multi-e-beam Cerenkov FEL. 500 kV relativistic electron beams at 280 A were introduced into a rectangular multi-dielectric cavity to yield 1.7 MW of output power at 33.4 GHz. This output frequency agrees well with the theoretical Cerenkov FEL frequency of 35.3 GHz.[11] Furthermore, it obviously deviates from the dependency of frequency upon magnetic guiding field. This confirms that the signal is Cerenkov coherent stimulated emission.

We must point out that when the sensitivity of the crystal detector was tested, the detector voltage corresponding to an input power of 30.5 mW was only 49 mV. This is far less than the 150 mV signal detected in the real measurement. Because of the saturation effect of the crystal detector, we know that the actual output of the Cerenkov FEL oscillator is higher than 1.7 MW. Furthermore, since most electrons collide with the metal absorber in the interaction zone, the efficiency is not very high. Improvement needs to be made to optimize the position of the guiding magnetic field relative to the laser oscillator to allow most electrons to pass. Thus, the power output and interaction efficiency can be further improved. More work in this area is under preparation.

References

1. P. A. Cerenkov, DOKL. AKAD. NAUK. SSSR, 14, 451 (1934).

2. Qingyuan Wang, et al., PHYS. REV. A, submitted on 24 Nov 1990.

3. J. E. Walsh, et al., PHYS. FLUID, 20 (4), 709 (1977).

4. K. L. Felch, et al., APPL. PHYS. LETT., 38 (8), 601 (1981).

5. S. Von Laven, et al., APPL. PHYS. LETT., 41 (5), 408 (1982).

6. E. Garate, et al., J. APPL. PHYS., 58 (2), 627 (1985).

7. William Main, et al., APPL. PHYS. LETT., 55 (15), 1498 (1989).

8. E. P. Garate, et al., NUCL. INSTR. AND METH., A259, 125 (1987).

9. J. Walsh, et al., NUCL. INSTR. AND METH., A272, 132 (1988).

10. Qingyuan Wang, et al., INTEL. J. IR&MM WAV., 10 (7), 889 (1989).

11. E. P. Garate, et al., IEEE J. QE-23 (9), 1627 (1987).

On-Line Measurements of Pulsed Electron Beam Emittance

92FE0307D Chengdu QIANG JIGUANG YU LIZI SHU [HIGH POWER LASER AND PARTICLE BEAMS] in Chinese Vol 3 No 4, Nov 91 pp 512-518

[Article by Zhu Dajun [4376 1129 6511], Huang Sunren [7806 1327 0088], and Liu Xisan [0491 6932 0005] of the Institute of Applied Electronics, CAEP: "On-Line Measurements of Pulsed Electron Beam Emittance"; MS received 18 Sep 90, revised 16 Jan 91]

[Text] Abstract

The design and testing of an on-line pulsed electron beam (e-beam) emittance measurement device are presented. The physical basis and the automatic data acquisition and processing process are described. Emittance measurements were performed in FEL experiments without a guiding magnetic field on the EPA-74 pulsed accelerator. The non-normalized emittance obtained was in the 0.3-0.7 mm-rad range. This device will be used to measure beam emittance on the SG-1 FEL.

Key Words: emittance, beam distribution.

I. Introduction

Emittance is the major indicator characterizing the quality of an e-beam. Beam quality (low emittance and low energy dispersion) is the determining factor for high FEL pumping efficiency and high power output. Theoretically, in order to ensure effective overlap between e-beam and light beam to promote interaction, the non-normalized emittance ε should be as close to the laser wavelength λ as possible. The shorter the wavelength becomes, the more rigorous this requirement is. In order to obtain an intense beam of low emittance, anode and cathode parameters must be selected carefully and the structure of the beam transport system and the focusing mode must be carefully designed.

There is some degree of technical difficulty involved in measuring the emittance of a single pulse. Although such measurements were done on devices such as ETA, FXR and ATA in the mid-1980's using the pepper-pot method,[1] this is the first time it has ever been used in China. In January 1988, the emittance of a 2 MV beam was first measured with an X-ray film.[2] Afterward,

the film technique was used at the Institute of Fluid Dynamics of the Chinese Academy of Sciences to measure the emittance on a 1.5 MeV linear induction accelerator.[3] That method essentially determines beam radius and angle of divergence by analyzing the density of an array of holes. The data processing is slow and the measurement is not real-time. The new method measures the fluorescence of a phosphor screen after the beam hits it. A camera is used to record the event and the data is digitized for computer processing. It can measure emittance real-time and is very convenient to use.

II. Definition of Emittance and Principle of On-Line Measurement

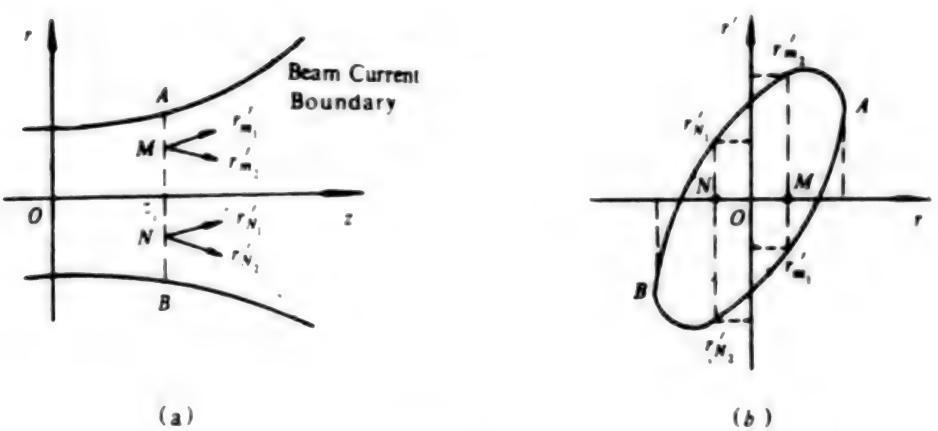
Earlier, the angle of divergence was used to express beam divergence. Later, the concept of emittance was introduced to beam physics. As shown in Figure 1, the state of particle motion can be described by the slope of the particle's radial position r_i and the direction of motion, i.e., dr_i/dz (or r_i'). On the phase plane (r, r'), it forms an ellipse with all the particles enclosed in it. We define emittance as area A over π:

$$\varepsilon = \frac{\iint dr\,dr'}{\pi} = \frac{A}{\pi} \tag{1}$$

Emittance decreases as particle energy increases. If particle momentum is also taken into account, then we can define a normalized emittance as

$$\varepsilon_n = \beta\gamma\varepsilon \tag{2}$$

where β is the relativistic velocity of the particle and γ is the relativistic factor. Based on theory, a particle has an important property: its normalized emittance remains constant during acceleration or transmission under ideal conditions.



(a) (b)

Figure 1

(a) beam current in divergence; (b) beam current phase chart at $z = z_0$ section

Usually, all the particles should be contained inside a six-dimensional super ellipsoid V_6 (x, x', y, y', z, z'). The ellipse on the phase plane is merely a projection of this ellipsoid on the phase plane (r, r'). Hence, equation (1) is usually called the boundary emittance ε.

Since particles are not uniformly distributed on (r, r'), in order to express the effect of beam distribution ρ (r, r') on emittance, a root-mean-square emittance concept is introduced:

$$\varepsilon_{rms} = 4\sqrt{\langle r^2\rangle\langle r'^2\rangle - \langle rr'\rangle^2} \qquad (3)$$

where "< >" represents an average over particle distribution; $\langle r^2\rangle$, $\langle r'^2\rangle$ and $\langle rr'\rangle^2$ are related to beam width, velocity distribution and beam divergence, respectively.

On plane (r, r'), beam distribution usually does not have an apparent boundary. In actual measurement, a percent emittance is defined. An area near 90 percent of the beam boundary is used instead of the total phase area. It is denoted as $\varepsilon_{e0.9}$. Three classical beam distributions were investigated theoretically:

(1) K-V distribution, where particles are uniformly distributed on the super ellipsoid surface, as well as in real geometric space. We get $\varepsilon_{rms} = \varepsilon_e$.

(2) W-B distribution, where particles are evenly distributed inside the super ellipsoid and follow a parabolic distribution in real geometric space. We have $\varepsilon_{rms} = 2\ \varepsilon_e/3 = 0.67\ \varepsilon_e$.

(3) GS distribution, where particles obey a Gaussian distribution in the super ellipsoid and in real geometric space; we have $\varepsilon_{rms} = 0.87\ \varepsilon_{e0.9}$. Obviously, it is more desirable to consider the mathematical distribution. W-B distribution has the lowest emittance.

Based on the principle of the pepper-pot plate technique to measure emittance, Shi Jiangjun [2457 1412 0689] did a detailed theoretical analysis.[4] The basic physics of on-line measurement are briefly discussed here. The scheme is established on the basis of e-beam → light → electric signal conversion and computer data processing. The unique feature is to use a conventional camera (non-CCD and silicon target) to record a transient emission picture and then digitize and store the data.[5]

1. Linear conversion from e-beam → phosphor screen → camera.

Linear conversion from e-beam to optical signal, from optical signal to video electric signal, all the way until A/D conversion of all the points on the picture, is the basis for data analysis.

When the e-beam hits the phosphor screen, the brightness of the screen is proportional to the incident current density:

$$L_n = KJ \tag{4}$$

where L_n is the brightness, J is the current density and K is a proportionality constant.

The emission characteristic of the phosphor screen is shown in Figure 2 [photograph not reproduced]. The afterglow is greater than 1 ms. The brightness-to-electricity conversion characteristic curve of the Vidicon camera is shown in Figure 3. It is linear. The A/D conversion has 64 gray levels and is also linear.

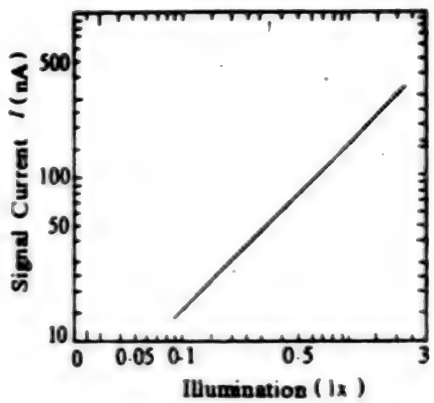


Figure 3. Brightness-to-Electricity Characteristic Curve

2. Temporary Storage in Camera

A transient picture (50 ns pulse) needs to be recorded, digitized and stored. However, it takes 40 ms to scan a picture. We are not using any storage devices. Instead, we chose to use a Vidicon tube which has a larger inertia. The target surface is made of a photoconductor. When light shines on the target, the production and dissipation of carriers are not instantaneous. Carriers have a fixed lifetime which causes a lag in photoconductance and makes it linger a while longer. This photoconductance inertia is dependent upon the target material, processing technique and illumination. If there is a light insulator dielectric layer, the charge storage time is even longer. As for the lag effect in the single sweep mode, it can be solved by trigger delay.

3. The digitization and storage of images are realized by a frame memory. Digitized data is used for processing by computer.

4. The phosphor screen should have a reference scale to specify the size of the image on the monitor. This system uses the outside frame of the phosphor screen as a reference scale.

IV. Experimental Setup

The experimental setup of the entire system is shown in Figure 4. The e-beam emitted by the cathode passes through the collimating aperture on the anode and enters the focusing lens interaction zone first and then reaches the emittance measurement system. The system is comprised of two major components: the emittance measurement system and the image recording and processing system. The emittance measurement system is designed to obtain a clear and crisp image on the phosphor screen. The lens area is 16 mm in diameter and the measurement chamber has an inner diameter of 50 mm. The spacing between the pepper-pot plate and the cathode is 40.8 cm. Our test showed no magnetic field penetration into this chamber. A magnetic shield is used to ensure that the magnetic field on the cathode surface is zero. The pepper-pot plate is made of graphite, and has a 7 x 7 array of holes. There are two kinds of pepper-pot plates, one with 0.5-mm-diameter holes and the other with 1-mm-diameter holes. The holes are 5.0 mm apart. The distance L between the pepper-pot plate and the phosphor screen is 5.0 cm. The beam elements are allowed to expand freely before hitting the fluorescent material (45-mm-diameter, 1-mm-thick phosphor or 0.1-mm-diameter aluminum foil with fast light sensitive screen stuck on the back). If the images from these small holes do not overlap, the divergence angle of the beam can be measured. If they do overlap, the cross section distribution of the beam can be determined. Image conversion and processing are carried out by a video camera, image memory and computer, as shown in Figure 5.

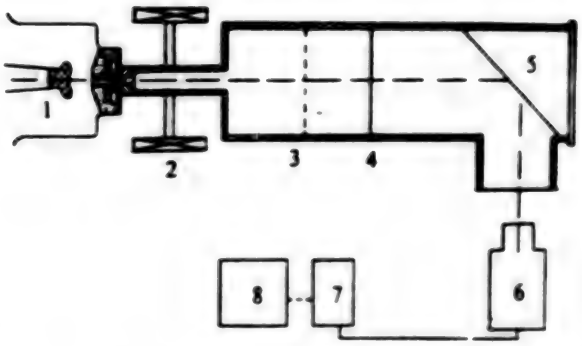


Figure 4. Beam Emittance Measurement System

1. cathode; 2. magnetic lens; 3. pepper-pot plate; 4. phosphor screen; 5. mirror; 6. camera; 7. monitor; 8. IBM/XT

The image corresponding to the moment of strongest light intensity can be recorded by adjusting the delay for image frame storage. Experimentally, it was determined that the system requires a 70 ms delay.

V. Automatic Acquisition, Storage and Processing of Data

Figure 6 shows a block diagram for data acquisition, storage and processing. A high-resolution video camera is used to scan every other line of the phosphor screen from top to bottom. The video signal is digitized and stored

in the image memory system for processing. The result can be displayed on a monitor or printed out by a printer.[6]

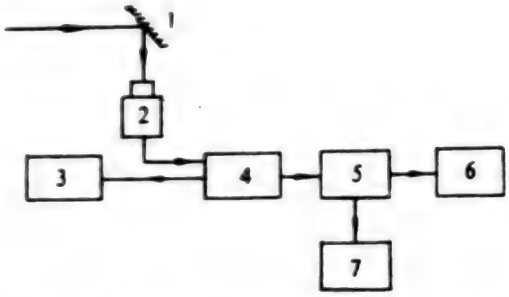


Figure 5. Emittance Measuring on the Line

1. mirror; 2. camera; 3. monitor; 4. memory (512 x 512.6 bits); 5. computer; 6. screen; 7. printer

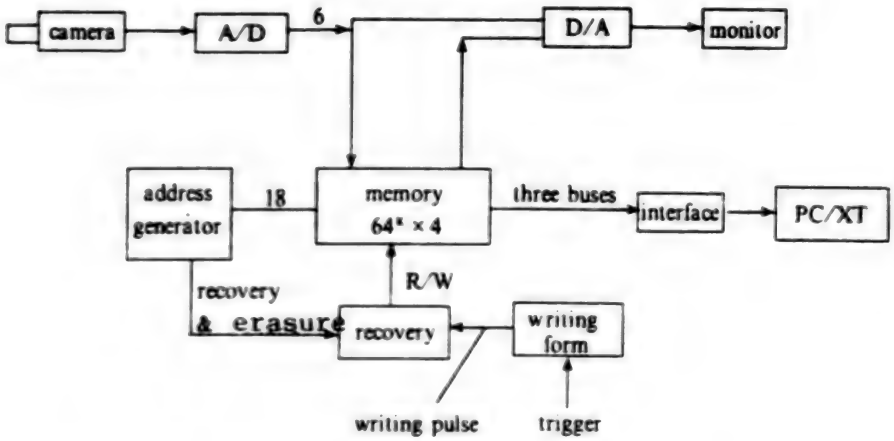


Figure 6. Obtaining and Storing Pictures

The function of the data processing software is to conduct a series of calculations on the intensity values corresponding to the image (512 x 512 pixels) in order to derive emittance and its phase diagram. The software package includes 11 software programs written in assembly language and FORTRAN, primarily for image data reconstruction, image display, cut-and-paste, beam coordinate and current intensity distribution, emittance phase diagram and emittance computation, printing, etc.

When operating the instrument, a static point needs to be adjusted to produce a clear horizontal image on the screen. Then, interference from an external light source is eliminated to minimize the background. After e-beams are generated by the accelerator, transient spot pictures can be seen on the monitor. They are captured in memory and processed by the computer. An image may be displayed on the itor again from the computer. Figure 7 [photograph not reproduced] reproduction of the spot picture shown on the monitor in experim nt r 3430. Figure 8 shows the three-dimensional

beamlet intensity. Figure 9 shows the intensity distribution along the spot coordinate in the x-direction for the second row of spots (from up down). Figure 10 shows the emittance phase diagram.

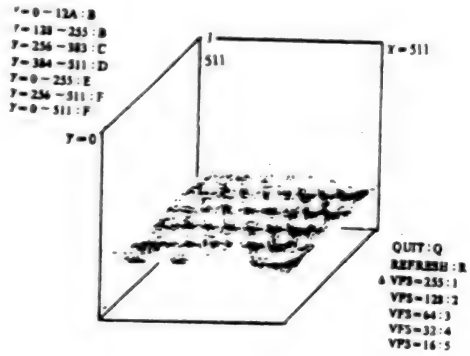


Figure 8. Three-Dimensional Drawing of Beamlet Intensity

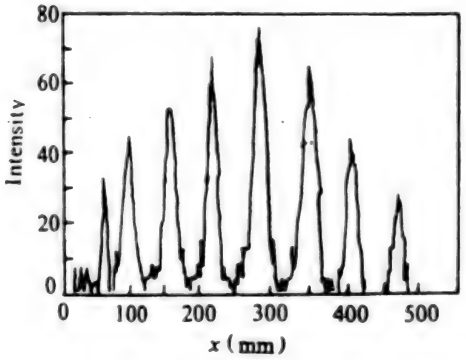


Figure 9. Intensity Distribution at Center Line

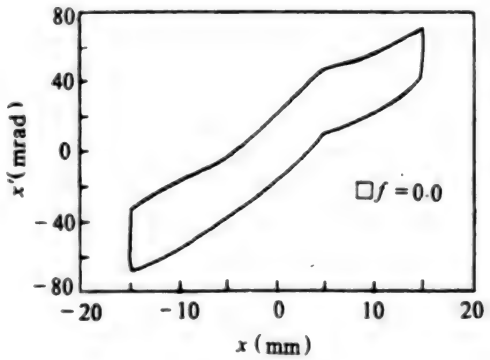


Figure 10. Phase Chart of Half-High Width Emittance

VI. Experimental Results and Analysis

We employed three data processing techniques to obtain emittance:

1. Emittance is calculated by phase space volume. Each beamlet is cut off at half maximum in determining the boundary coordinate and divergence angle. All points on the phase plane are connected by straight lines to find the area. The value of emittance is ε = 0.338 mm-rad.

2. Beam radius is determined by the envelope width at half maximum. It is then multiplied by the average half divergence angle which is determined by the half maximum width of each beamlet. We get ε = 0.334 mm-rad.

3. Obtain the beam distribution boundary by cutting into equal density. Define a percentage $f = \rho/\rho_m$ where ρ_m is the highest peak of all the beamlets. At different f values, the angles of divergence are obtained by finding two boundaries for each spot, as shown in Figure 11. Emittance can be obtained

by finding the corresponding area. When f = 0, the emittance is the highest; $\varepsilon_{e(t=0)}$ = 0.605 mm-rad.

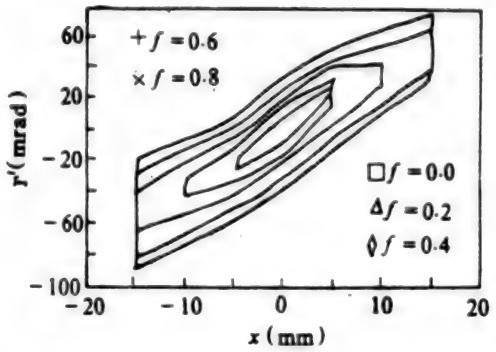


Figure 11. Emittance Phase Chart at Different f Cutting

Figure 12 shows the relation between emittance and f. It is normalized to ε_e with W-B distribution and to 3 ε_c with GS distribution. ε_c is a constant emittance. The measured emittance is $\varepsilon_{e(t=0)}$. The figure shows that measured emittance values are closer to the curve calculated using Gaussian distribution.

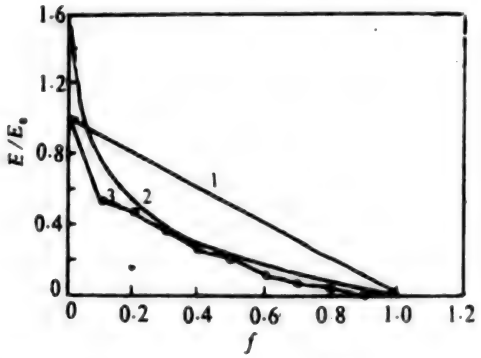


Figure 12. Curves With Different Distributions

1. WB distribution; 2. Gaussian distribution; 3. experimental data

The following is a discussion of the experimental results.

1. Reliability of experimental data.

The maximum emittance the instrument can determine is $\varepsilon \sim 3$ mm-rad based on the parameters chosen. The minimum resolution of emittance $\delta\varepsilon \sim 0.02$ mm-rad. The measured result is 1/10th of the maximum and 10 times the minimum resolution. This proves that the design is appropriate. We used an array of 0.5-mm-diameter holes with 2 mm spacings. After 5 cm of drift, spots were not found to overlap. Based on this observation, ε should be less than 0.4 mm-rad. This is in agreement with the result described earlier. By means of

numerical computation using the envelope equation, as shown in Figure 13, the parameters are I = 450 A, $\beta\gamma$ = 1.93 and R_0 = 0.65 cm. The calculation shows that only a beam envelope of $\varepsilon_{rms} \leq 0.4$ mm-rad can pass through a 16-mm-diameter, 17-cm-long tube. Therefore, this is consistent with our measured result.

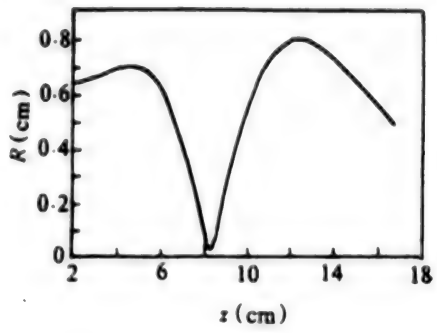


Figure 13. Typical Envelope Curve in Magnetic Lens Region

2. Error analysis.

Major sources of error include precision of hole size, effect of space charge, angular resolution of the camera and non-linearity of the conversion system. The error of hole size plays the most critical role.

In measurement and data processing, there is some degree of scatter in emittance. Some may differ by 50 percent. This is primarily due to unstable diode emission; difference in phase diagram between rows of holes, i.e., difference in cross section area at different y cutting point in the three-dimensional phase space (x, x', y) where the projection area is the maximum cross section area; and signal weakening due to a time interval of 20 ms between scanning alternate lines.

3. This is the first experiment and there are improvements to be made. For example:

Beam off-center: to make beam axis, magnetic axis and tube axis concentric.

Measure a series of separation points (i, r', ρ) to fit a beam distribution ρ(r, r') and then derive the rms emittance rigorously from equation (3).

Improve the sensitivity of the camera tube, lower background noise level and enhance the beam intensity distribution in order to raise resolution.

Acknowledgement: The image storage and processing system was contracted to and supplied by Beijing University. Xia Songjiang [1115 2646 3068], Wang Shuyuan [3769 2885 0337], and Lu Jianqin [0712 1696 2953] helped in the testing of the experimental system. Zhang Shichang [1728 6624 2490] of the Institute of Electrical Engineering provided the plastic phosphor screen. The authors are grateful to all the people mentioned above.

References

1. "Measurement of Emittance and Cross Section Beam Current Density of ATA Injector," UCID-19839, 1983.

2. He Wenlong [0149 2429 7893], "Definition and Measurement of Emittance," Thesis, February 1988.

3. Cheng Nianan [4153 1819 1344], "Measurement of Emittance of Intense E-Beam Pulse," QIANG JIGUANG YU LIZI SHU [HIGH POWER LASER AND PARTICLE BEAMS], Vol 1, No 3, 1989, p 241.

4. Shi Jiangjun [2457 1412 0689], "E-Beam Brightness and Principle of Measuring Emittance With Pepper-Pot Plate," QIANG JIGUANG YU LIZI SHU [HIGH POWER LASER AND PARTICLE BEAMS], Vol 1, No 4, 1989, p 344.

5. Li Xisan et al., "Measurement of Emittance of Intense E-Beam," August 1987.

6. Zhu Dajun, "Measurement of Beam Emittance and Its Relation to Current Transport," Thesis, March 1990.

Beam Quality Improvement Using Collimating Apertures

92FE0307E Chengdu QIANG JIGUANG YU LIZI SHU [HIGH POWER LASER AND PARTICLE BEAMS] in Chinese Vol 3 No 4, Nov 91 pp 525-529

[Article by He Peiai [0149 1014 5337], Cheng Nianan [4453 1819 1344], He Wenlong [0149 2429 7893], and Tao Zucong [7118 4371 5115] of the Institute of Fluid Physics, China Academy of Engineering Physics: "Beam Quality Improvement Using Collimating Apertures"; MS received 5 Oct 90, revised 19 Nov 90]

[Text] Abstract

A method for obtaining high-quality intense electron beams by using a collimating aperture in conjunction with adjusting the guiding magnetic field is described. This method was tested on a 1.5 MeV linear induction accelerator (LIA). The resultant beam was found to have much less energy spread and several times higher brightness. In addition, radial distribution of beam density and brightness were measured.

Key Words: beam brightness, collimating aperture.

I. Introduction

Both free electron laser (FEL) and flash X-ray photography require a high-brightness electron beam (e-beam) with minimal energy dispersion from an LIA. The beam brightness data obtained in the past on a 1.5 MeV LIA[1,2] only reflects the time integral effect for various electron energy levels. The brightness of a beam with minimal energy dispersion (corresponding to the plateau of the accelerating pulse voltage) was accurately measured. Particularly corresponding to the leading and trailing edge of the pulse, beam energy varies considerably. Large energy dispersion may cause beam brightness to deteriorate severely. Therefore, eliminating or reducing the beam corresponding to the leading and trailing edge of the pulse can improve beam quality.

Based on the transport characteristics, it is possible to remove low-energy electrons from the beam by using a collimating aperture and by adjusting the guiding magnetic field. Not only is the beam spread reduced, but also its energy dispersion is improved. The result is a more ideal collimated beam with better quality. This method is easy to implement and the effect is

obvious. Different-size collimating apertures may be used based on the magnitude of the beam.

II. Principle and Method

In an LIA, the motion of an electron with charge e and mass γm can be described by Lorentz law:

$$\frac{dP}{dt} = e\left[E + \frac{1}{c}(v \times B)\right] \tag{1}$$

where P = γmv is the relativistic momentum, $\gamma = (1 - \beta^2)^{-1/2}$, $\beta = |v|/c$, v is the electron velocity, c is the speed of light, and E and B are the macroscopic electric field and magnetic field, respectively.

Considering under axial symmetry that $|v_\theta|$, $|v_r| << |v_z|$, $|B| \approx B_z$, the radial equation of motion of the beam can be derived from equation (1).[3]

$$\ddot{r}_b + \frac{\dot{r}_b\dot{\gamma}}{\gamma} + \left(\frac{eB_z}{2\gamma mc}\right)^2 r_b = \frac{e}{\gamma m}\left(E_r - \frac{v_z B_\theta}{c}\right) + \frac{(p_\theta/m)^2}{\gamma^2 r_b^3} \tag{2}$$

where r_b is the radius of the beam envelope. Each subscript represents the corresponding component, "·" represents the time derivative, and p_θ/m is a kinetic constant.

When an e-beam travels at a speed of v_z in an invariant magnetic field B_0 in vacuum, if the kinetic energy of the beam remains constant as well, then equation (2) becomes

$$\ddot{r}_b + \left(\frac{\Omega}{2\gamma_0}\right)^2 r_b = \frac{e}{\gamma_0 m}(E_r - \beta_0 B_\theta) + \frac{(p_\theta/m)^2}{\gamma_0^2 r_b^3} \tag{3}$$

where field component E_r and B_θ are dependent upon the beam charge density n. They are determined by Gauss's theorem and Ampere's law.

$$\oint E \cdot dS = 4\pi e \int n dV \tag{4}$$

$$\oint B \cdot dl = \frac{4\pi e}{c} \int nv \cdot dS \tag{5}$$

For a beam with fixed radius r_b and density n, we have the following from equations (3), (4) and (5):

$$\ddot{r}_b + \left(\frac{\Omega}{2\gamma_0}\right)^2 r_b - \frac{\omega_p}{2\gamma_0} r_b = \frac{(p_\theta/m)^2}{\gamma_0^2 r_b^3} \tag{6}$$

where $\Omega = eB_0/m$ is spin frequency, $\omega_p = (4\pi n_0 e^2/m)^{1/2}$ is the beam plasma frequency.

Equation (6) shows that the electric field of the beam itself causes the beam to expand. B_0, on the other hand, exerts force in the opposite direction to balance its radius:

$$r_{b0}^2 = \frac{2p_e/m}{(\Omega^2 - 2\omega_p^2/\gamma)^{1/2}} \tag{6'}$$

The general solution of equation (6) oscillates. Equation (6') usually varies due to variation of the guiding magnetic field or other electrical disturbance. Assuming r_b is comprised of r_{b0} and oscillation radius δr and knowing the total beam current $I = \pi r_b^2 n_0 e\beta_0 c$ which is independent of r_b, the following can be derived from equation (6):

$$\delta\ddot{r} + [(\frac{\Omega}{\gamma_0})^2 - \frac{\omega_p^2}{\gamma^3}]\,\delta r = 0 \tag{7}$$

Equation (7) has a sinusoidal solution with the following frequency:

$$\omega = [(\frac{\Omega}{\gamma})^2 - \frac{\omega_p^2}{\gamma^3}]^{1/2} \tag{8}$$

Based on this equation, the e-beam travels like a wave with a wavelength of $\lambda = 2\pi\beta c/\omega$. The magnitude of λ is determined by the beam energy and axial guiding magnetic field. Similar results were obtained in the simulation of high-intensity e-beam transport.

Since electrons have different energies in the beam, their corresponding wavelengths are also different. When a collimating aperture is present in the path, some electrons are eliminated because they are at their peaks and some can pass through the aperture because they are at their valleys. Thus, it is possible to obtain collimated beams of different energies by adjusting the guiding magnetic field or pulse voltage.

In the series of derivations, the effect of beam leading edge and initial position, total beam current conservation and beam density as a function of radius, and equations of beam envelope and beam trajectory are not explored in detail. Further study is required. Despite this fact, the derived result is found to be applicable to the 1.5 MeV LIA.

Figure 1 shows the beam current and pulse voltage versus time curves in the 1.5 MeV LIA. Based on the timing, electrons at the plateau of the pulse have higher energy, less energy spread and more stable beam brightness. Using the method described earlier, this portion of the beam should be allowed to pass the collimating aperture as much as possible in order to eliminate electrons corresponding to the leading and trailing edge; this results in a high-quality collimated beam.

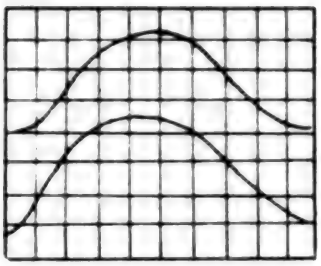


Figure 1. Waveform of Pulse Beam Current (upper) and Pulse Voltage (lower)

III. Experimental Setup

Figure 2 shows the experimental setup. The collimating aperture remains stationary and its aperture R_c is adjustable. Beam current I_b and collimated beam current I_b' are measured with CVRs. The pepper pot, fluorescent screen, reflective mirror and camera behind the collimating aperture are used to measure the emittance of the collimated beam. The ferrite circle is used to shield the magnetic field generated by the solenoid to improve the accuracy of emittance measurement.

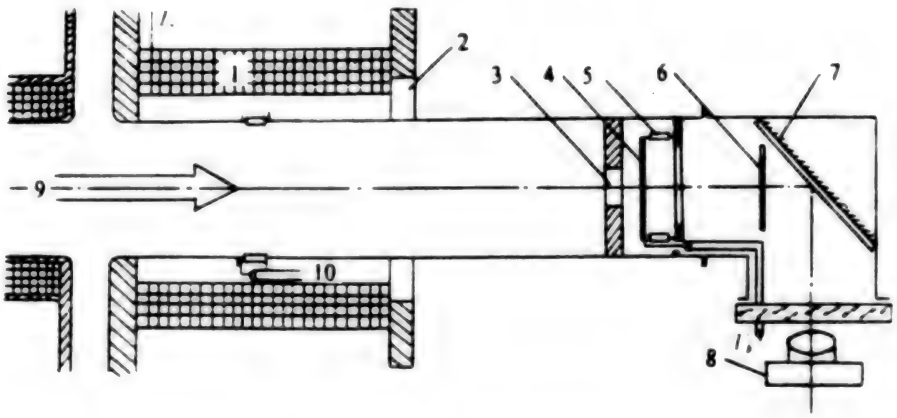


Figure 2. Scheme of the Experiment

1. solenoid; 2. ferrite circle; 3. collimator aperture; 4. pepper pot; 5. CVR; 6. fluorescent screen; 7. reflective mirror; 8. camera; 9. electron beams; 10. I_b CVR

The pepper pot consists of 7 x 7 holes. The diameter and thickness are 1 mm. Since the collimating aperture is very close to the pepper pot, the radius of the aperture can be considered as the beam radius. Although the CVR for beam current I_b is some distance apart from the CVR of the collimated beam current I_b', it still has the effect of a guiding magnetic field. I_b loss can be neglected. A more detailed description of emittance measurement can be found in reference 1.

IV. Experimental Results and Brief Analysis

Experimentally, two criteria have been established for the collimated beam I_b'. (1) In order to have maximum collimated beam output, timewise, it should correspond to the plateau of the voltage pulse. (2) It should be able to repeat I_b' many times with a good plateau and spread. We conducted tests in the following three areas despite the fact that each test is very complicated (varying a parameter requires several tests to yield a suitable value):

1. Adjust the axial guiding field (expressed in terms of the excitation current I_7) while keeping pulse voltage (beam energy) constant and collimating aperture R_c at 20 mm. When the magnetic field varies, the collimating current waveform also changes. Figure 3 shows three sets of typical waveforms for I_b' and I_b as the magnetic field decreases. However, the optimal collimated current profile is not illustrated in this figure.

The collimated current shown in Figure 3(b) is apparently more ideal. The magnetic fields corresponding to Figures 3(a) and 3(c) are either too high or too low. A comparison of the waveforms of I_b and I_b' shows significant improvement at the leading and trailing edges and the plateau.

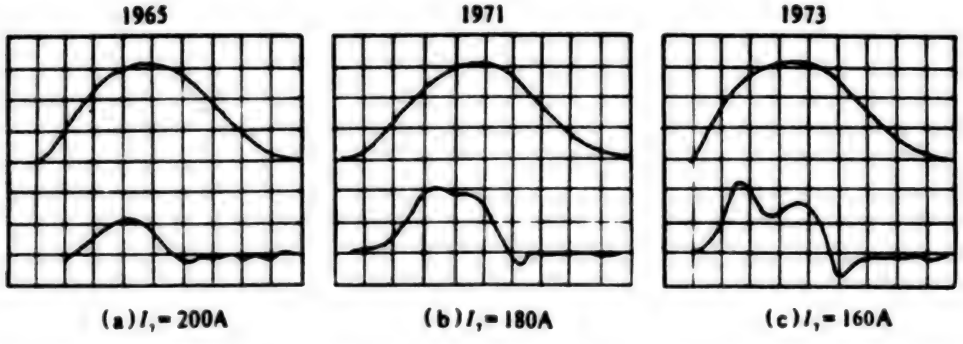


Figure 3. Waveforms of Beam Current (upper) and Collimated Beam Current (lower) for Different Magnetic Field

2. Vary the accelerating voltage while leaving the magnetic field unchanged and keeping R_c at 30 mm. Similarly, the waveform for I_b' varies a great deal. Figure 4 shows three typical cases as the voltage falls. It is similar to the situation as we adjust the magnetic field.

3. At the same accelerating voltage, vary R_c and adjust the magnetic field to obtain the optimal I_b' output. In addition, measure the rms emittance ε_{rms}, normalized brightness B_n and mean beam current density $\bar{\sigma}$ for different R_c values. The results are shown in Table 1 and Figure 5.

As one can see, the brightness of I_b' varies significantly with the collimating aperture R_c and guiding magnetic field. A more ideal brightness can be obtained by adjusting these two parameters. The beam density σ follows a Gaussian distribution with R_c, consistent with work done abroad.

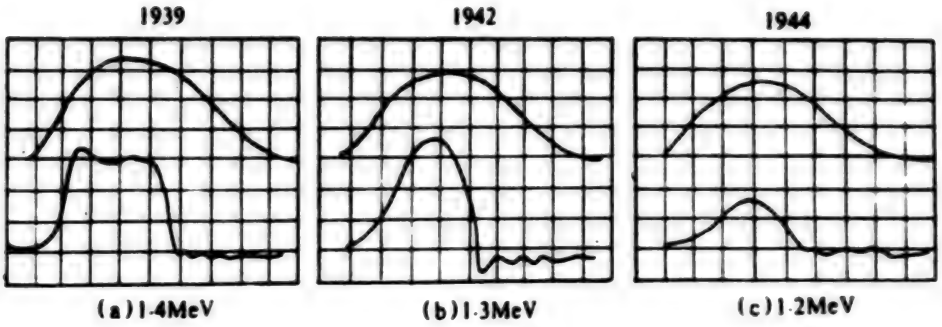


Figure 4. Waveforms of Collimated Beam Current I_b' (lower) for Different Voltage (upper)

Table 1. Values of ε_{rms}, B_n and $\overline{\sigma}$ for Different Radii of Collimator

R_c (cm)	I_b (A)	ε_{rms} ($\times 10^{-4}$ m·rad)	ε_n ($\times 10^{-4}$ m·rad)	B_n ($\times 10^7$ A/m^2 · rad^2)
1.0	690	1.08	1.08	11.90
1.5	1540	1.98	1.99	7.80
2.0	1600	2.50	2.34	5.83
3.0	2000	5.32	5.36	1.39

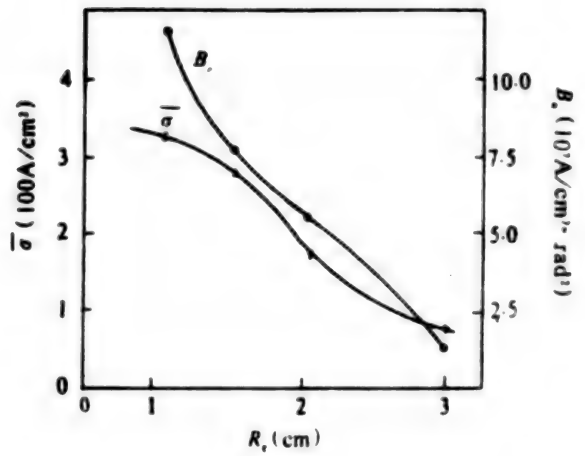


Figure 5. Distribution Curves of B_n and $\overline{\sigma}$ for Different Radii

Of course, based on Figures 3 and 4, the collimated current I_b' is still not ideal in terms of plateau, pulse width and spread. Two possible factors affecting the outcome are: (1) non-linearity of the guiding magnetic field might have affected the laminar nature of the beam, and (2) stability of the accelerator might be less than desirable. We might not have obtained the optimal parameters with limited number of tests. More work is still required.

V. Conclusions

1. By using a collimating aperture and adjusting the guiding magnetic field, it is possible to reduce the energy spread and improve the leading and trailing edge of the e-beam to enhance its brightness.

2. This method was used on a 1.5 MeV LIA and the radial distributions of beam density and brightness were obtained. The fact that beam density follows a Gaussian distribution indicates that within a certain range its brightness can be significantly increased by reducing R_c.

References

1. Cheng Nianan, "Summary of Emittance Measurements on 1.5 MeV LIA," Symposium on Intense-Current Linear Induction Accelerators, CAEP, 1989.

2. He Wenlong et al., "Measurement of Intense E-Beam Brightness Using Magnetic Collimator," QIANG JIGUANG YU LIZI SHU [HIGH POWER LASER AND PARTICLE BEAMS], Vol 2, No 2, 1990.

3. B. R. Miller, "Physics of Intense Charged Particle Beams," 1985.

Electromagnetic-Wave-Pumped FEL Studied

92FE0362A Beijing DIANZI KEXUE XUEKAN [JOURNAL OF ELECTRONICS] in Chinese
Vol 13 No 6, Nov 91 pp 603-610

[Article by Yin Yuanzhao [1438 0337 3507] of the Institute of Electronics, the Chinese Academy of Sciences: "A Free Electron Laser Pumped by Electromagnetic Wave," a project supported by the National Natural Science Foundation; MS received 4 Oct 90, revised 25 Feb 91]

[Excerpts] Abstract

An electromagnetic-wave-pumped FEL (free electron laser) is studied. A large-radius electron beam (e-beam) from a magnetic cusp passes through a cylindrical waveguide and interacts with the TE_{11}-mode incident electromagnetic wave of the waveguide. By using the Vlasov distribution theory and three-dimensional waveguide equation, the dispersion relation of scattered waves in the Compton region is deduced. Based on numerical analysis, the growth rate and frequency of scattered waves as a function of axial guiding magnetic field, e-beam energy, electron cyclotron ratio and radial position of the electron ring are discussed.

Key Words: free electron laser (FEL), electromagnetic-wave-pumped, cylindrical waveguide, guiding magnetic field.

I. Introduction

FELs can generate coherent emission from millimeter wave to visible light. The FEL is being rapidly developed as a tunable high-power laser. Most FEL studies use a static magnetic wiggler.[1-3] This work uses a traveling-wave wiggler, i.e., an electromagnetic wave traveling with respect to the relativistic e-beam for pumping to produce coherent emission from the back-scattering of the e-beam.[4] Compared to a static magnetic wiggler, the electromagnetic wiggler has two advantages. First, the wavelength of a static magnetic wiggler cannot be made short enough due to technical limitations. When the wavelength is shortened, the axial magnetic field strength also decreases. In order to increase its strength, it is necessary to reduce the aperture of the wiggler. In order to generate the same electronic transverse velocity perturbation, the magnetic field for the static wiggler, B_w(kGs), and the power density of the pumping electromagnetic wave,

P_{EM} (MW/cm^2), can be converted as follows: $P_{EM} = 60\ B_w^2$. When $B_w = 1$ kGs, $P_{EM} = 60$ MW/cm^2. Hence, the electromagnetic wiggler has a very high power requirement. However, due to advances in areas such as gyrotrons,[5] CARM [cyclotron auto-resonance maser] and the wiggler-free FEL,[6] it is no longer difficult to produce a high-power large-aperture electromagnetic wave source on the order of a few to a few dozen MW with wavelength as short as the millimeter or sub-millimeter range. Thus, we are no longer limited to using a static wiggler. It is possible to employ a low-energy e-beam to produce a coherent emission at a very short wavelength. Next, because the same e-beam is used to produce a coherent emission at a very short wavelength, the concept of a two-stage FEL[7] has attracted a great deal of attention. The second stage involves electromagnetic wave pumping. The theoretical treatment presented in this paper would apply to this case. [passage omitted]

V. Numerical Analysis and Discussion

From the dispersion equation (22), the frequency and wave number of the scattered wave are determined by the dispersion of the waveguide:

$$\omega_2^2 - c^2k_{\parallel}^2 - c^2k_{r2}^2 = 0 \tag{25}$$

and the dispersion of the e-beam wave which is produced by the pumping wave and the scattering wave is:

$$\omega - v_{\parallel}k - l\Omega_s = 0 \tag{26}$$

Equations (25) and (26) can be solved simultaneously by using equation (6).

$$\left.\begin{aligned} \omega_2 &= \gamma_{\parallel}^2\beta_{\parallel}[\Omega_c/\beta_{\parallel} \pm (\Omega_c^2 - c^2k_{r2}^2/\gamma_{\parallel}^2)^{1/2}] \\ k_2 &= (\gamma_{\parallel}^2/c)[\beta_{\parallel}\Omega_c \pm (\Omega_c^2 - c^2k_{r2}^2/\gamma_{\parallel}^2)^{1/2}] \end{aligned}\right\} \tag{27}$$

where

$$\gamma_{\parallel} = (1 - \beta_{\parallel}^2)^{-1/2},\quad \Omega_c = \omega_1 + (l_1 + l_2)\Omega_s + v_{\parallel}k_1.$$

In order to obtain the growth rate of the scattering wave, let $\omega_2 = \omega_r + i\omega_i$, $\omega_r > \omega_i$. Here, ω_r is ω_2 in equation (27). We shall only discuss the high-frequency case corresponding to +. Substituting it into the dispersion equation (22), we obtain

$$\omega_i = [\sqrt{3}\,c/(4R_0)]\{[\omega_p c\tilde{A}_1/(\gamma_0 R_0)]^2 S_1 S_2/(2D_{l2}\omega_2\Omega_{l1}^2\Omega_{l2})\}^{1/3} \tag{28}$$

Figure 1 shows several curves of growth rate ω_i versus orientation angle modulus l_2; the curves correspond to a number of radial positions of the e-beam ring R_0 when the e-beam energy E = 1.5 MeV and axial magnetic field $B_{\parallel} = 1$ kGs. Although l_2 is an integer, for ease of observation, the points are connected as continuous curves. Figure 2 shows the relation of ω_2, l_2 and electron cyclotron ratio α (corresponding to the maximum growth rate ω_{imax} shown in Figure 1) as a function of R_0. Here, we define $\alpha = \beta_{\perp 0}/\beta_{\parallel}$ as

the ratio of the angular to axial velocity ratio when the electron ring is in equilibrium. From Figures 1 and 2, as R_0 increases, α gets larger, and ω_{imax} also rises and shifts toward the direction of larger l_2. In the meantime, the frequency corresponding to ω_{imax}, ω_2, also increases. This is a very exciting result. It points out that the electron ring should be as close to the waveguide wall as possible. We must point out that the half width a of the electron ring remains unchanged in the calculation. Hence, when R_0 increases, the filling factor F also goes up. However, the effect of F on gain enhancement and field distribution is relatively small.

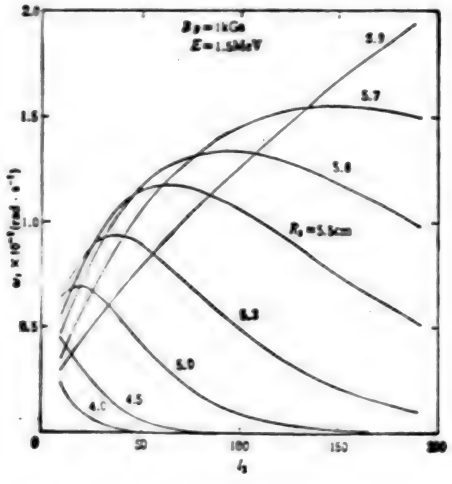


Figure 1. Growth Rate Vs. Orientation Angle (at different electron ring radial positions); $\omega_1 = 6 \times 10^{10}$ rad·s^{-1}, $k_1 = 0.396$ cm^{-1}, $l_1 = 10$, $P_w = 50$ MW, a = 0.1 cm, total current of electron ring = 5 kA, $R_w = 6$ cm.

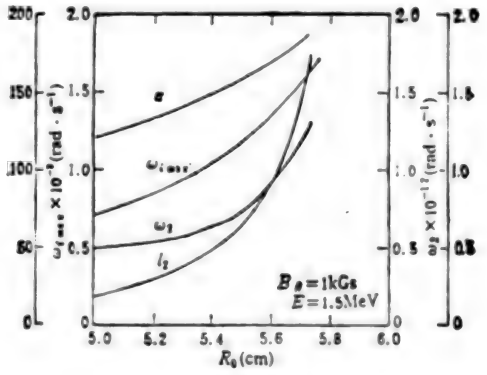


Figure 2. Growth Rate, Frequency, Orientation Angle Modulus and Cyclotron Ratio at Maximum Values in Figure 1 vs. Radial Position of Electron Beam (other parameters identical to those in Figure 1)

Figure 3 shows how ω_{imax}, its corresponding frequency ω_2, orientation angle modulus l_2 and cyclotron ratio α vary with e-beam energy E when the axial magnetic field $B_{//}$ remains constant. Now that $B_{//}$ = 1 kGs, when E → 1.21 MeV, $\alpha \to \infty$. This means that when the electron ring has no axial drift, $v_{\theta 0} = v_0$ and $v_{//} = 0$. From Figure 3, as E increases from 1.21 MeV, α falls rapidly, ω_{imax} declines slowly, ω_2 rises, and l_2 remains unchanged.

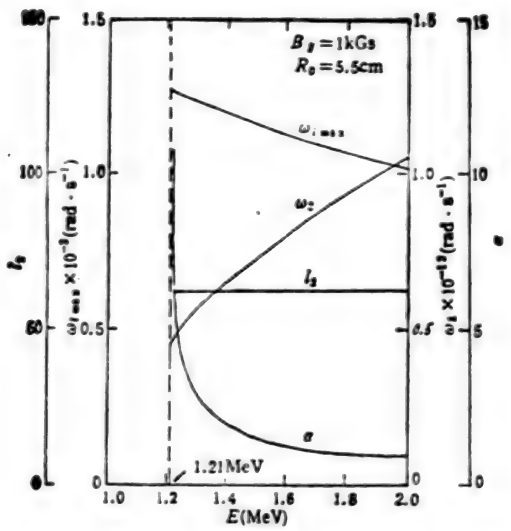


Figure 3. Maximum Growth Rate, Frequency, Orientation Angle Modulus and Cyclotron Ratio vs. Electrom Beam Energy; $B_{//}$ = 1 kGs, other parameters identical to Figure 1

Figure 4 shows how ω_{imax}, its corresponding frequency ω_2, orientation angle modulus l_2 and cyclotron ratio α vary with the axial magnetic field $B_{//}$ when the e-beam energy E remains constant. Now that E = 1.5 MeV, when $B_{//}$ rises from 1.18 kGs, α gradually increases and rapidly approaches infinity, l_2 gradually increases until reaching a constant level, and ω_{imax} and ω_2 show peak values. From Figures 3 and 4, one can see that when the axial magnetic field remains unchanged, if the cyclotron ratio is increased, the growth rate goes up and the frequency falls. When the e-beam energy is constant, both growth rate and frequency reach their maximum values in a certain axial magnetic field. When both e-beam energy and axial magnetic field remain constant, growth rate and frequency will increase when the electron ring is close to the cylindrical waveguide wall.

The growth rate calculated in this work is lower than that obtained with a static wiggler.[10,11] Because the current density used is not high enough:

$$\omega_i = 5.4 \times 10^3 \text{rad} \cdot \text{s}^{-1}$$

Compared to the values given in references 10, 11, this is approximately four orders of magnitude lower. The pumping power is also not high enough; the power density is approximately two orders of magnitude lower than that

used in references 10, 11. If these factors are taken into account, then the growth rate will go up by approximately four orders of magnitude, close to those reported in references 10, 11.

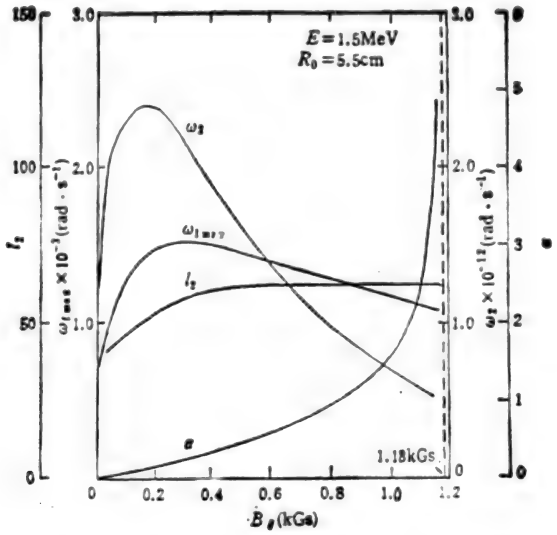


Figure 4. Maximum Growth Rate, Frequency, Orientation Angle Modulus and Cyclotron Ratio vs. Axial Magnetic Field; E = 1.5 MeV, other parameters identical to Figure 1

In order to demonstrate the characteristics of a low-energy electron ring, Figure 5 is presented as an example. Comparing Figure 3 to Figure 5, the low-energy growth rate is slightly larger than the high-energy growth rate. However, the frequency is slightly lower. There is no substantial difference between the two. Nevertheless, it is far more convenient to use a low-energy electron ring in practice.

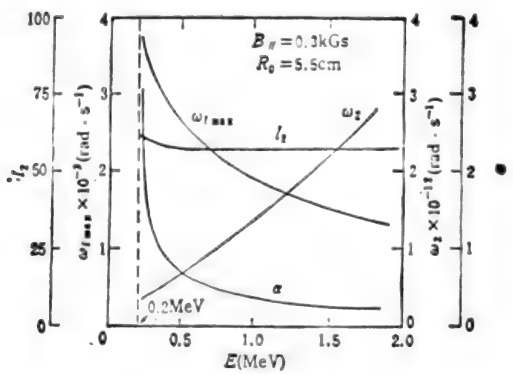


Figure 5. Maximum Growth Rate, Frequency, Orientation Angle Modulus and Cyclotron Ratio vs. E-Beam Energy; $B_{//}$ = 0.3 kGs, other parameters identical to Figure 1

VI. Conclusions

Using a cyclotron electron ring from a magnetic cusp in electromagnetic wave pumping has the following advantages. First, with properly selected parameters, it is possible to make the growth rate go up by increasing the electron cyclotron ratio. The axial magnetic field not only confines the e-beam to prevent it from diverging, but also makes the beam circle in a large radius to increase the effective range for electron-wave interaction. This makes the growth rate go up and makes it possible to reduce the length of the laser. This is similar to the situation with a static wiggler.[10,11] Next, when the electron ring gets closer to the waveguide wall, both growth rate and frequency increase. Third, with properly selected parameters, it is possible to use a low-energy e-beam to produce radiation at a frequency close to that generated with a high-energy e-beam. Therefore, the structure introduced in this paper may be used to make a compact low-voltage FEL.

References

1. S. H. Gold, et al., PHYS. FLUIDS, 27 (1984), 746.

2. T. J. Orzechowski, et al., IEEE J. OF QE, QE-21 (1985), 831.

3. W. W. Destler, et al., PHYS. FLUIDS, 28 (1985), 1962.

4. R. Alan Kens, et al., IEEE TRANS. ON PS, PS-18 (1990), 437.

5. K. E. Kreischer, et al., IEEE TRANS. ON PS, PS-13 (1985), 364.

6. S. H. Gold, et al., IEEE TRANS. ON PS, PS-13 (1985), 374.

7. Y. Carmel, et al., PHYS. REV. LETT., 51 (1983), 566.

8. M. J. Rhee, W. W. Destler, PHYS. FLUIDS, 17 (1974), 1574.

9. N. M. Kroll, W. A. McMullin, PHYS. REV., A17 (1978), 300.

10. Y. Z. Yin, G. Beketi, PHYS. FLUIDS, 28 (1985), 1186.

11. Y. Z. Yin, R. J. Ying, G. Bekefi, IEEE J. OF QE, QE-23 (1987), 1610.

Nation's First EMW-Pumped FEL Experimental System Completed

92P60152A Chengdu SICHUAN RIBAO in Chinese 6 Feb 92 p 1

[Article by SICHUAN RIBAO staff writer: "Nation's First 'Electromagnetic-Wave-Pumped Free Electron Laser Experimental System' Built in Sichuan"]

[Text] After a 4-year effort, a University of Electronic Science and Technology research group led by Profs. Liu Shenggang [0491 4141 4854] and Liang Zheng [2733 2973] and Associate Research Fellow Li Jiayin [2621 1367 5255] recently completed at the university the nation's first "electromagnetic-wave-pumped (EMW-pumped) free electron laser (FEL) experimental system." In the system, they used a 3-cm pumping wave and a 600-keV-energy electron beam to generate a 3-mm-band FEL. This type of tunable-frequency laser has important applications in biomedicine, materials science, and a number of cutting-edge research areas.

100-Watt High-Repetition-Rate XeCl Excimer Laser Developed

92P60170A Beijing ZHONGGUO DIANZI BAO [CHINA ELECTRONICS NEWS] in Chinese 28 Feb 92 p 1

[Article by Wei Baozhi [7614 0202 5347]: "High-Power Excimer Laser Developed"]

[Summary] The "100-watt high-repetition-rate XeCl excimer laser" developed by the CAS Anhui Institute of Optics and Fine Mechanics (AIOFM) as a State Seventh 5-Year Plan priority project recently passed the technical appraisal held by CAS and the State Education Commission. Via measurements conducted at the China Institute of Metrology and the China University of Science and Technology, the AIOFM-developed excimer laser was found to have a maximum output average power of 109 watts and a maximum monopulse energy of 569 millijoules, fully meeting the requirements in the state's contract specifications. The experts agreed that this new laser would be a useful tool in the further development of high-tech research and in the further expansion of laser applications.

100J-Class KrF Excimer Laser Passes CNNC-Organized Expert Appraisal

92P60196A Beijing ZHONGGUO KEXUE BAO [CHINESE SCIENCE NEWS] in Chinese
17 Mar 92 p 2

[Article by Chang Jiachen [1603 3946 6591]: "Krypton Fluoride Excimer Laser Output Energy Reaches 100 Joules"]

[Summary] A China Research Institute of Atomic Energy Sciences research group led by Prof. Wang Ganchang [3769 3227 2490] and Prof. Wang Wanyan [3769 8001 1750], after a 3-year-plus effort, has succeeded in raising the output energy of its KrF excimer laser to 100 joules. On 2 March in Beijing, this achievement passed the expert technical appraisal organized by the China National Nuclear Corporation (CNNC). The expert panel, led by China Academy of Engineering Physics (CAEP) Prof. Du Xiangwan [2629 4382 3834], gave this achievement its highest evaluation.

This laser, which has a wide variety of applications including inertial confinement fusion, industry, and medicine, originally had an output energy of 13 J, but the scientists were able to overcome a variety of technical hurdles in raising this value to 30 J, then to 80 J, and finally to 100 J by the end of 1990. Since then, they have engaged in debugging and perfecting the technique. With this achievement, China joins a select group of nations such as the United States, Japan, and Great Britain that have been able to develop 100J-class KrF excimer lasers in the laboratory.

Tapered Wiggler Technique Used in Low-Energy-E-Beam Raman FEL

92P60211A Shanghai ZHONGGUO JIGUANG [CHINESE JOURNAL OF LASERS] in Chinese Vol 19 No 1, Jan 92 pp 22-26

[Article by Zhao Donghuan [6392 2639 3562] and Wang Jian [3769 1696] of the Shanghai Institute of Optics & Fine Mechanics, CAS, Shanghai 201800: "Application of Tapered Wiggler Technique in Low-Energy-Electron-Beam Raman Free Electron Laser"; MS received 24 Apr 91, revised 18 Jun 91. Project supported by NSFC.]

[Abstract] Expressions for the Raman FEL efficiency are deduced by means of ponderomotive potential, the effect of a tapered wiggler technique on enhancement of FEL efficiency is analyzed, and an experiment with a tapered-wiggler-field Raman FEL is conducted. In the experiment, the tapered-wiggler field intensity device is a 1.44-m-long tapered double-helix tube with a helical face taper of 0.3°, a double-helical line diameter of 3.5 mm and composition of enamel-insulated wire, a helical period of 24 mm, and a total of 60 coils. Initial-to-final-end field intensity ratio $B_w(0)/B_w(L)$ is 2.56. The guide magnetic field intensity (B_0) is 12.4 kG. Coherent radiated energy measured by the calorimeter under optimal operating conditions was 668 mJ, radiation wavelength was in the 8-10.4-mm range, and the output peak power was 31 MW. Since the 0.45 MeV injected e-beam had a power of 320 MW (I = 800 A, V = 0.4 MV), the calculated efficiency is 9.68 percent, or 2.6 times the value of 3.7 percent obtainable with a 1.3-m-long fixed-wiggler Raman FEL[7]. While this result lags behind that obtained by the Lawrence Livermore National Laboratory[5], it must be noted that the LLNL scientists used an intermediate-energy (4.5 MeV) e-beam for their experiment, while the present experiment employed a low-energy (0.45 MeV) e-beam.

All four figures are reproduced below.

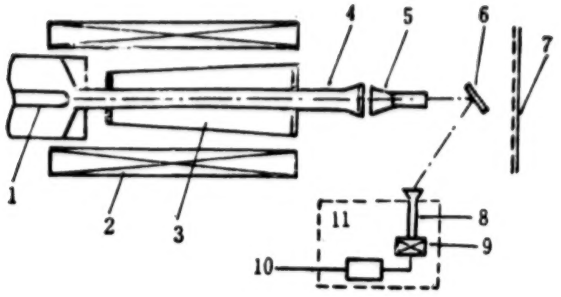


Figure 1. Schematic of Experimental Setup of a Raman FEL

1. diode; 2. guide magnetic field solenoid; 3. tapered wiggler; 4. drift tube; 5. calorimeter; 6. mirror; 7. microwave absorbent; 8. waveguide; 9. test system of millimeter wave; 10. oscillograph; 11. shielding house

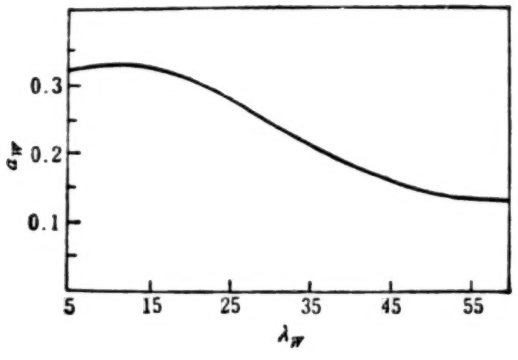


Figure 2. Vector Potential Profile of the Tapered Wiggler Field

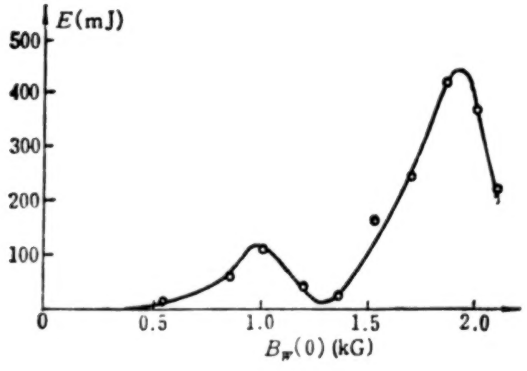


Figure 3. Emittance Energy vs. Wiggler Magnetic Field $B_w(0)$ at the Guide Magnetic field B_0 of 12.4 kG

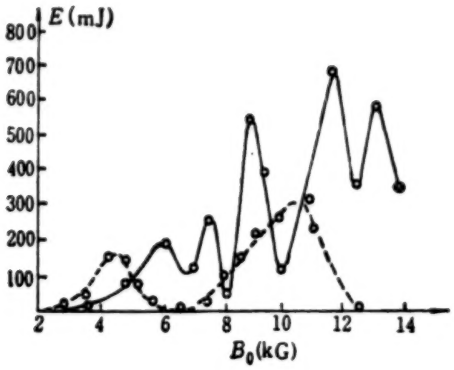


Figure 4. Emittance Energy Measured vs. Guide Magnetic Field; solid line is the measured result at tapered wiggler magnetic field, dotted line is the measured result at constant wiggler magnetic field

References

[1] Liu Shenggang, QIANG JIGUANG YU LIZI SHU [HIGH-POWER LASER AND PARTICLE BEAMS], 2(2), 131 (1990).
[2] N.M. Kroll et al., IEEE J. QUANT. ELECTR., QE-17, 1436 (1981).
[3] A. Bhowmik et al., IEEE J. QUANT. ELECTR., QE-21, 998 (1985).
[4] R.H. Jackson et al., IEEE J. QUANT. ELECTR., QE-19, 346 (1983).
[5] T.J. Orzechowski et al., PHYS. REV. LETT., 57(17), 2172 (1986).
[6] Tian Shihong et al., QIANG JIGUANG YU LIZI SHU [HIGH-POWER LASER AND PARTICLE BEAMS], 2(4), 467 (1990).
[7] Lu Zaitong et al., GUANGXUE XUEBAO [ACTA OPTICA SINICA], 9(9), 780 (1989).

- END -

END OF FICHE

DATE FILMED

13 May 1992